JACS Au
AN OPEN ACCESS JOURNAL OF THE AMERICAN CHEMICAL SOCIETY
Open Access

pubs.acs.org/jacsau
Article

NH_3-Induced Challenges in CO_2 Hydrogenation over the Cu/ZnO/Al_2O_3 Catalyst

Xuan Bie, Yukun Pan, Xiaowei Wang, Shiyu Zhang, Jiahui Hu, Xiaoxiao Yang, Qinghai Li, Yanguo Zhang, Robert E. Przekop, Yayun Zhang,* and Hui Zhou*

Cite This: *JACS Au* 2025, 5, 1243−1257

Read Online

ACCESS | Metrics & More | Article Recommendations | Supporting Information

ABSTRACT: Gas sources rich in CO_2 derived from biomass/waste gasification, anaerobic digestion, or industrial carbon capture often contain impurities such as H_2S, H_2O, and NH_3, which can significantly hinder catalyst performance. Here, we show the role of NH_3 on the reverse water−gas shift (RWGS) reaction over a commercial Cu/ZnO/Al_2O_3 catalyst, examining its effects on both the catalytic activity and the catalyst structure. We found that NH_3 reversibly decreases CO_2 conversion immediately by suppressing carbonate hydrogenation and CO desorption. This effect intensifies with an increase in NH_3 concentration but decreases at higher temperatures. However, prolonged exposure (over 100 h) to RWGS conditions in the presence of 1.4% NH_3 leads to near-total and irreversible deactivation of the Cu/ZnO/Al_2O_3 catalyst. Under NH_3 exposure, the catalyst loses Cu^+ sites on the surface, causing a spatial separation of Cu and ZnO. Finally, to address this challenge, we propose a novel strategy to mitigate NH_3 inhibition by decomposing NH_3 into N_2 and H_2.

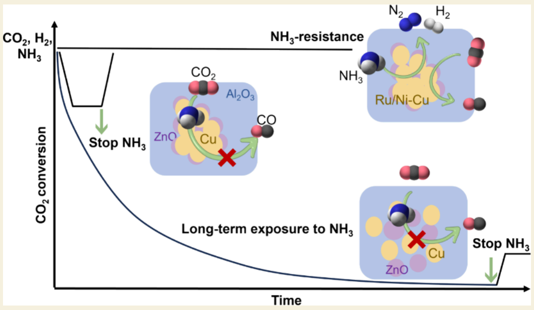

KEYWORDS: *CO_2 hydrogenation, impurity, deactivation, RWGS reaction, the role of NH_3, NH_3 decomposition*

INTRODUCTION

Since the Industrial Revolution, increasing levels of carbon dioxide in the atmosphere have driven anthropogenic climate change.[1] Consistent with the guidelines of the United Nations Framework Convention on Climate Change, many countries prioritize achieving carbon neutrality.[2] CO_2 hydrogenation to CO, commonly known as the reverse water−gas shift (RWGS) reaction, is among the most promising CO_2 conversion processes for CO_2 utilization.[3,4] The produced CO can be converted into various liquid fuels (gasoline, diesel, and methanol) via Fischer−Tropsch synthesis (FTS) and other syngas conversion processes.[5,6]

CO_2 streams derived from biomass/waste gasification, biomass/waste anaerobic digestion, carbon capture from power plants and steel plants, and other industrial processes[7−11] often contain impurities such as NH_3, H_2S, and H_2O.[12,13] For example, gas from biomass steam gasification typically contains 38−56% H_2, 17−32% CO, 13−17% CO_2, 1−150 g m^{-3} tar, 100−1400 ppm of NH_3, and 20−200 ppm of H_2S.[12] Additionally, trace amounts of NH_3 can occur in CO_2 streams from industrial carbon capture processes.[14,15] These impurities can act as catalyst poisons in CO_2 conversion processes.[16,17] Furthermore, the main capital costs of FTS are gasification and gas purification, and gas cleanup is particularly costly for biomass-to-liquid processes.[18] Therefore, establishing benchmarks for the tolerance of catalysts to specific poisons without significant deactivation can help determine the necessary gas cleaning requirements. This insight can contribute to the development of poison-resistant catalysts and the realization of cost-effective, environmentally friendly energy utilization.[19]

Some studies have reported the effects of H_2O and H_2S on CO_x hydrogenation processes.[20−23] For example, one study reported that 500 ppm of H_2S deactivated Cu/ZnO catalysts by forming ZnS, CuS, Cu_2S, and $CuSO_4$ phases.[23] In addition, a suitable amount of water (2.24 mol %) promoted methanol formation over Cu/ZnO/ZrO_2 catalysts during CO_2 hydrogenation by facilitating the hydrolysis of methoxy.[21] However, the role of NH_3 in the CO_2 hydrogenation processes has not been reported. Additionally, studies have shown that the effects of NH_3 on the FTS process may be contradictory.[24−26] NH_3 can adsorb onto and block cobalt sites, inhibiting the adsorption and activation of H_2, making ppm levels of NH_3 harmful to the FTS process using cobalt catalysts.[26] Furthermore, increasing the ammonia level (in the form of NH_4NO_3) to 400 ppm rapidly deactivated the Fe catalyst and simultaneously changed the product selectivities by oxidizing

Received: November 18, 2024
Revised: January 2, 2025
Accepted: January 6, 2025
Published: January 15, 2025

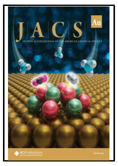

https://doi.org/10.1021/jacsau.4c01097

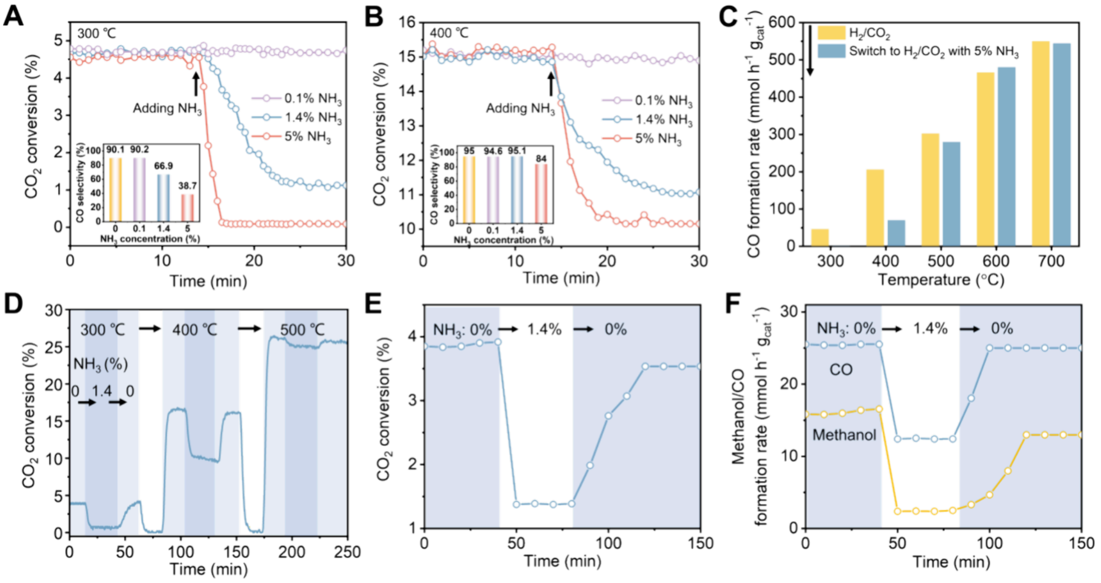

Figure 1. Role of NH_3 on the catalyst performance. (A) CO_2 conversion and CO selectivity over $Cu/ZnO/Al_2O_3$ at 300 °C and (B) at 400 °C (reaction conditions: 1 bar, H_2:CO_2:N_2 = 1:1:1, contact time: 0.05 s g/mL^{-1}). Inset: CO selectivity at different NH_3 concentrations. (C) CO formation rate during RWGS over $Cu/ZnO/Al_2O_3$ with 5% NH_3 addition (reaction conditions: 1 bar, H_2:CO_2:N_2 = 1:1:1, contact time: 0.05 s g/mL^{-1}). (D) Changes in CO_2 conversion when switching the gas composition (reaction conditions: 1 bar, H_2:CO_2:N_2 = 1:1:1, contact time: 0.05 s g/mL^{-1}). (E) CO_2 conversion and (F) methanol formation rate over $Cu/ZnO/Al_2O_3$ with 1.4% NH_3 addition for CO_2 hydrogenation to methanol (reaction conditions: 250 °C, 30 bar, H_2:CO_2:N_2 = 3:1:1, contact time: 0.03 s g/mL^{-1}).

χ-Fe_5C_2 to Fe_3O_4.[27] Conversely, recent studies have demonstrated the positive effects of NH_3 on the FTS process. NH_3 can reduce the secondary reactions of olefins and enhance the production of primary products, particularly olefins.[25] NH_3 has also been shown to expand the types of FTS products. For example, the formation of long-chained aliphatic amines, nitriles, and amides was promoted via exposure to 10% NH_3 over Fe-based catalysts.[28]

Cu-based catalysts, particularly $Cu/ZnO/Al_2O_3$, are widely used in CO_2 hydrogenation reactions owing to their excellent activity, selectivity, and low cost.[29−31] In this study, we investigated the role of NH_3 on the RWGS reaction activity and catalyst evolution over the $Cu/ZnO/Al_2O_3$ catalyst. We report that short-term tests revealed a significantly reversible inhibition of the CO_2 hydrogenation activity by NH_3. Operando diffuse reflectance infrared Fourier-transform spectroscopy (DRIFTS) and solid-state nuclear magnetic resonance (ssNMR) experiments revealed that NH_3 impeded carbonate hydrogenation and CO desorption. Moreover, NH_3 competed with CO_2 and H_2 for adsorption on the catalyst surface. Exposure to a H_2/CO_2 system containing 1.4% NH_3 for 100 h resulted in complete deactivation of the $Cu/ZnO/Al_2O_3$ catalyst. To elucidate the deactivation mechanism, changes in active metal states, catalyst structure, and physicochemical properties were investigated. Our findings indicate that the presence of NH_3 in the gas flow led to the eventual disappearance of Cu^+ sites on the catalyst surface, causing the separation of Cu and ZnO and a consequent loss of redox properties. Finally, we designed a series of ammonia-resistant catalysts to counteract the inhibitory effect of NH_3 in the RWGS reaction.

RESULTS

Alteration of the RWGS Reaction Pathway by NH_3 Addition

The CO_2 hydrogenation process was conducted in a tubular fixed-bed reactor (Figure S1). In the absence of a catalyst, the conversion of CO_2 was low (Figure S2). In this study, the Cu and ZnO loadings in the industrial $Cu/ZnO/Al_2O_3$ catalyst were 58.2 and 29.6 wt %, respectively, as determined via inductively coupled plasma−optical emission spectroscopy (ICP-OES) (Table S1). The catalyst was initially reduced in situ under a 5% H_2/N_2 flow at 500 °C for 2 h (with a heating rate of 10 °C min^{-1}) before the RWGS reaction. $Cu/ZnO/Al_2O_3$ exhibited high performance, approaching thermodynamic equilibrium, when NH_3 was absent in the reaction gas under temperatures of 300−700 °C and a H_2/CO_2 ratio of 1:1 (Figures S3 and S4). The introduction of 0.1% NH_3 had a minimal impact on the reaction (Figure 1A). However, increasing the NH_3 concentration to 1.4% inhibited CO_2 conversion from 4.4 to 0.9% at 300 °C and reduced the CO selectivity from 90.1 to 66.9%. Additionally, solid byproducts were observed at the reactor outlet and identified as ammonium carbonate ($(NH_4)_2CO_3$) and ammonium bicarbonate (NH_4HCO_3) through X-ray diffraction (XRD) analysis (Figures S5 and S6). Increasing the NH_3 concentration to 5% resulted in nearly complete catalyst deactivation, with the CO_2 conversion dropping to 0.06% and a substantial decrease in the CO selectivity and the CO formation rate at 300 °C (Figure 1A,C). This indicates that the catalytic activity decreases with increasing NH_3 concentrations, while the CH_4 formation rate remains largely unaffected, suggesting distinct formation mechanisms for CO and CH_4 (Figure 1C and Figure S7). Additionally, the impact of NH_3 was mitigated at higher temperatures (Figure 1A−C and Figure S3). Increasing the temperature from 300 to 400 °C led to a 5.5% reduction in CO_2 conversion caused by the presence of 5% NH_3 (from 15.6

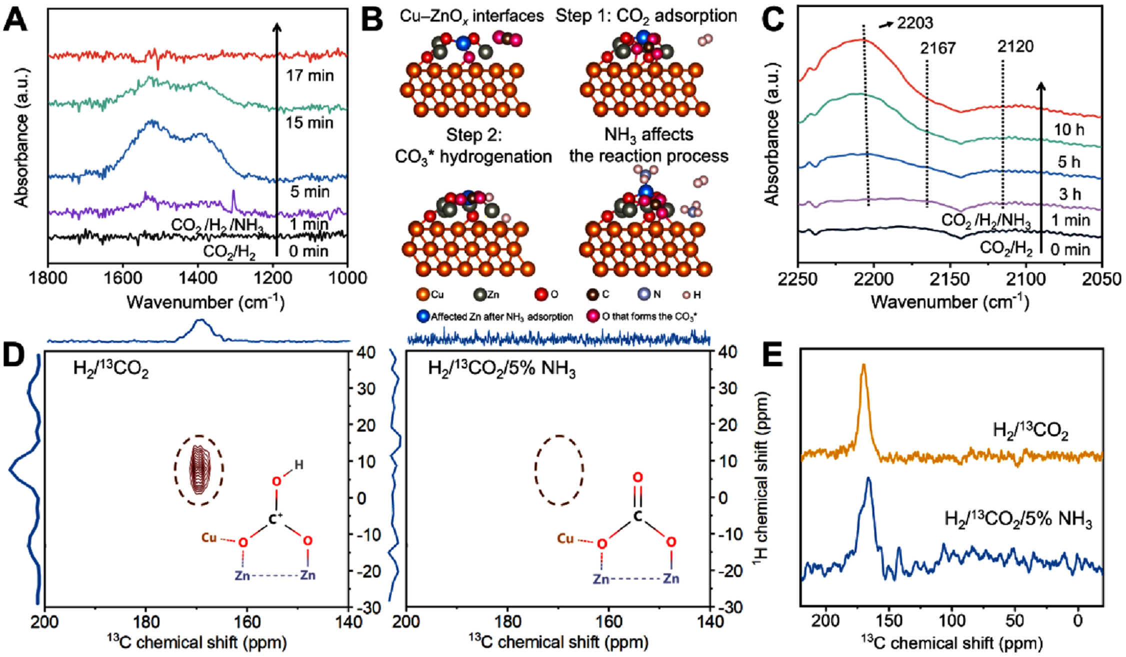

Figure 2. Evolution of reactive intermediates as detected via operando DRIFTS and ssNMR. (A) Evolution of the surface functional groups over Cu/ZnO/Al$_2$O$_3$ (reaction conditions: 400 °C, 5% H$_2$/5% CO$_2$/0.2% NH$_3$/N$_2$) in 17 min. (B) Illustration of NH$_3$ hindering carbonate hydrogenation. (C) Evolution of carbonyl groups over Cu/ZnO/Al$_2$O$_3$ (reaction conditions: 400 °C, H$_2$:CO$_2$:N$_2$ = 1:1:1 with 1.4% NH$_3$) during 10 h of TOS. (D) Ex situ MAS NMR ^{1}H−^{13}C HETCOR spectra of Cu/ZnO/Al$_2$O$_3$ exposed in H$_2$/^{13}CO$_2$ or H$_2$/^{13}CO$_2$/5% NH$_3$ (reaction conditions: 400 °C, 4 h, H$_2$:^{13}CO$_2$ = 1:1). (E) Ex situ DD-MAS NMR ^{13}C spectra of Cu/ZnO/Al$_2$O$_3$ exposed to H$_2$/^{13}CO$_2$ or H$_2$/^{13}CO$_2$/5%NH$_3$ (reaction conditions: 400 °C, 4 h, H$_2$:^{13}CO$_2$ = 1:1).

to 10.1%) (Figure 1B). Notably, the RWGS was not significantly inhibited by NH$_3$ at temperatures above 500 °C (Figures S3 and S8, vide infra). The inhibitory effect of NH$_3$ was reversible in short-term tests (less than 60 min), as demonstrated by adding NH$_3$ to the reactor for a specific period and then stopping its introduction (Figure 1D and Figure S9).

We also investigated the effects of contact time and the H$_2$/CO$_2$ ratio on NH$_3$ inhibition (Figures S10 and S11). Notably, increasing the contact time reduced the inhibitory effect of NH$_3$, while NH$_3$ inhibition was observed across all H$_2$/CO$_2$ ratios from 1:1 to 4:1. Furthermore, increasing the H$_2$/CO$_2$ ratio enhanced the inhibitory effect of NH$_3$ on the RWGS reaction. Additionally, we tested the role of NH$_3$ in CO$_2$ hydrogenation to methanol at 30 bar and 250 °C with a H$_2$:CO$_2$:N$_2$ ratio of 3:1:1 (Figure 1E,F and Figure S12) and found that NH$_3$ similarly acted as a reversible poison in the process. Specifically, the presence of 1.4% NH$_3$ resulted in a significant decrease in the level of CO$_2$ conversion from 3.9 to 1.4%, a reduction in methanol selectivity from 38.3 to 16.1%, and a decrease in the methanol formation rate from 16.0 to 2.4 mmol h^{-1} g$_{cat}$$^{-1}$. This indicates the broad inhibitory effect of NH$_3$ on the CO$_2$ hydrogenation reactions (vide infra).

To elucidate the instantaneous deactivation mechanism caused by NH$_3$ addition during the RWGS reaction, we conducted in situ DRIFTS experiments to investigate the evolution of the reaction intermediates. The in situ-reduced Cu/ZnO/Al$_2$O$_3$ catalyst was first subjected to CO$_2$ (30 mL min^{-1}) preadsorption for 30 min, followed by a 60 min N$_2$ purge before the DRIFT spectra were collected (Figure S13). Bands at 1538, 1476, 1395, and 1362 cm^{-1} were observed, indicating the formation of carbonate species on the Cu−ZnO$_x$ interface.[32−34] After the gas was switched to H$_2$, the carbonates were rapidly consumed, leading to the formation of CO and H$_2$O within 5 min. Notably, when the gas was switched to 1.4% NH$_3$/N$_2$ instead of H$_2$ (Figure S14), carbonates were also consumed, indicating a reaction between NH$_3$ and CO$_2$.

To monitor real-time intermediates under the reaction conditions, we further employed operando DRIFTS to investigate surface intermediates on the catalyst. Under an H$_2$/CO$_2$/N$_2$ flow (5/5/90) at 400 °C, no distinct bands were observed (Figure 2A), indicating the rapid consumption of intermediates. Upon switching from a 5% H$_2$/5% CO$_2$ flow (lasting for 60 min) to a 5% H$_2$/5% CO$_2$/0.2% NH$_3$ flow, carbonate bands began to appear within 1 min, reached their maximum intensity after 5 min, and then gradually faded, disappearing after 17 min (Figure 2A). It indicates that the introduction of NH$_3$ initially hindered carbonate hydrogenation, attributed to the initial decrease in catalyst activity (Figure 2B). Studies have reported that adsorbed NH$_3$ negatively affects dissociative H$_2$ adsorption,[26,27] which may explain why NH$_3$ hindered carbonate hydrogenation in this study. After 5 min, an equilibrium between NH$_3$ and H$_2$ on the catalyst surface was achieved, leading to the gradual consumption of carbonates and stabilization of the reaction activity. This trend was also observed in experiments with the effect of NH$_3$ on CO$_2$ hydrogenation to methanol. The results further elucidate the impact of NH$_3$ on carbonate hydrogenation processes (Figure 1E,F).

Furthermore, we tested NH$_3$ adsorption on the catalyst with and without the reaction stream. An in situ DRIFTS experiment conducted solely under 1.4% NH$_3$ conditions revealed weak adsorption of NH$_3$ on the catalyst surface. This observation is consistent with the results from NH$_3$ temperature-programmed desorption (NH$_3$ TPD) and NH$_3$ DRIFTS (Figures S15−S17). In contrast, pronounced NH$_3$ adsorption occurred when a similar operando DRIFTS experiment was conducted under $H_2/CO_2/N_2$ (1:1:1) with 1.4% NH_3 for 10 h. The products were simultaneously quantified via gas chromatography (GC) (Figure S18). During the 10 h time on stream (TOS), a rapid decline in catalytic activity was observed at the initial stage. Bands corresponding to NH_3 species on Cu/Zn sites (1623 cm^{-1}), NH_4^+ species on Zn−OH sites (1423 and 1340 cm^{-1}), and NH_3 species on Zn sites (1260 and 1234 cm^{-1}) emerged (Figures S18−S20).[35,36] These findings highlight a pronounced affinity of NH_3 for the ZnO substrate under a CO_2-containing flow (for detailed discussions, see Figures S19−S21). This enhanced NH_3 adsorption on the catalyst surface further hindered the hydrogenation of the carbonates.

We also investigated the effect of NH_3 on carbonate hydrogenation using density functional theory (DFT) calculations. These calculations first established a stable configuration of the Cu−ZnO_x interface with adsorbed CO_2. The configuration was characterized by the stable bonding of oxygen atoms (from ZnO) to both Cu and adsorbed CO_2. The analysis highlighted that the strong adsorption of NH_3 on the Cu surface occupied the Cu atoms (with an adsorption energy of −0.72 eV, Table S2 and Figure S22), making it difficult for H_2 to adsorb near $^*CO_3$ and provide *H (with an adsorption energy of −0.06 eV, Table S2 and Figure S22). Consequently, subsequent reactions occurred between $^*CO_3$ and NH_3 or the decomposition products of NH_3. Additionally, the adsorption of NH_3 by Zn ions (blue atoms) at the Cu−ZnO_x interface affected the reaction intermediates (with an adsorption energy of −1.11 eV; see Figure 2B, Table S2, and Figure S22). Once NH_3 was adsorbed on $Zn^{\delta+}$, CO production became extremely difficult. Moreover, recent investigations have elucidated that HCOO* on the Cu surface serves as a critical intermediate in the formation of CH_4 rather than CO.[37,38] This delineates a potential pathway for methane synthesis, where the notably low rate of CH_4 formation implies that intermediates are present in minimal quantities, rendering them elusive to detection. The adsorption site of the HCOO* species (on the Cu surface) differed from that where the CO_3* species formed (at the Cu−ZnO_x interface). This distinction may explain the unaffected methane production. Additionally, the stability of HCOO* species, unaffected by a hydrogen-rich environment, coupled with NH_3 capacity to provide hydrogen, likely underpins the sustained production of CH_4 observed.[38]

In the CO adsorption DRIFTS experiment, the band at 2103 cm^{-1}, observed after N_2 purging, disappeared with the increase in temperature to 100 °C, indicating weak CO adsorption on the catalyst (Figure S23). During the CO_2 hydrogenation process, with or without NH_3, in situ DRIFTS revealed two bands at 2120 and 2167 cm^{-1}, corresponding to gas-phase CO (Figure 2C).[33] In the 10 h DRIFTS experiment with 1.4% NH_3, a new band emerged at 2203 cm^{-1}, which was absent under H_2/CO_2 conditions on the Cu/ZnO/Al_2O_3 catalyst (Figure 2C). Additionally, the NH_3 adsorption process in isolation did not manifest this band, indicating that the band is associated with species generated by the interaction between NH_3 and CO_2 (Figure S24). Thus, we ascribed the band to the *N═C═O (*NCO) species.[39,40] Subsequent in situ DRIFTS analysis on ZnO samples under a NH_3/CO_2 flow at 400 °C revealed a related band at 2210 cm^{-1}, while a similar examination of the Cu surface showed this band at 2200 cm^{-1} (Figure S25). This suggests that the *NCO species (2203 cm^{-1}) preferentially adsorbed at the Cu−ZnO_x interface rather than on isolated Cu or ZnO surfaces. Additionally, the $Zn^{\delta+}$ sites at the Cu−ZnO_x interface (blue atoms in Figure 2B) were the primary sites for NH_3 adsorption. The presence of *NCO species indicates that the formed CO* reacted with adsorbed NH_x species to produce *NCO species rather than desorbing as gas-phase CO. Consequently, the RWGS reaction was suppressed.

To gain deeper insights into changes in reaction intermediates during the RWGS reaction, we conducted isotopic labeling experiments. First, a mixture of $H_2/^{13}CO_2$ was subjected to the Cu/Zn/Al_2O_3 catalyst for 4 h at 400 °C. A separate catalyst was treated with a mixture of $H_2/^{13}CO_2$/5% NH_3 under similar conditions. Afterward, the system was cooled to room temperature and thoroughly purged with nitrogen. The resulting samples were carefully transferred into a specialized rotor within a glovebox to avoid exposure to air, and their magic angle spinning nuclear magnetic resonance (MAS NMR) spectra were recorded (Figure 2D,E and Figures S26 and S27). The $^1H-^{13}C$ cross-polarization (CP)-MAS NMR spectrum of the catalyst under NH_3-free condition showed a peak at 170 ppm (Figure 2D), which is attributed to bicarbonate or formate species.[41,42] However, in situ DRIFTS experiments revealed the absence of formate species (Figure S28), leading us to attribute it to bicarbonate species. This peak was absent in the $^1H-^{13}C$ CP-MAS NMR spectra of the catalyst exposed to the RWGS stream with 5% NH_3 (Figure 2D). To confirm the absence of carbonaceous species on the surface of this catalyst, a ^{13}C double quantum dipolar (DD)-MAS NMR spectrum was collected (Figure 2E). While the ^{13}C CP-MAS NMR signals are restricted to carbon nuclei near protons, the ^{13}C DD-MAS NMR technique does not have this limitation. Consequently, both CP-MAS and DD-MAS methods are often used to assess protonated and non-protonated carbons in carbonaceous materials.[43] The ^{13}C DD-MAS NMR analysis revealed a distinct signal at 166 ppm for the catalyst under 5% NH_3, attributed to carbonate species.[44] The results indicate that NH_3 inhibited carbonate hydrogenation, consistent with the findings from in situ DRIFTS.

NH_3-Induced Long-Term Deactivation of Cu/ZnO/Al_2O_3

To assess the long-term effect of NH_3 on the performance of Cu/ZnO/Al_2O_3, we subjected the catalyst to 100 h of TOS of RWGS at 400 °C under two conditions: in the absence of NH_3 and in the presence of 1.4% NH_3 (Figure 3). In the absence of NH_3, CO_2 conversion decreased from 15.7 to 13.7% over the 100 h period. In contrast, in the presence of 1.4% NH_3, the CO_2 conversion rapidly dropped from 16.0 to 11.8% within the

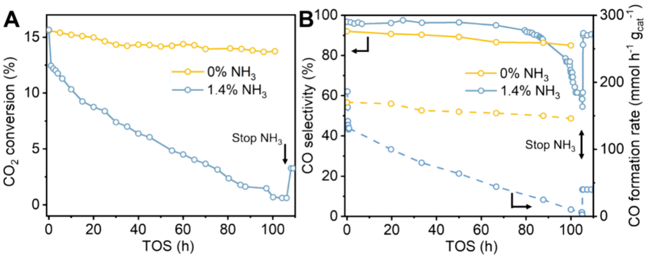

Figure 3. Role of NH_3in the stability test of RWGS. (A) CO_2 conversion and (B) CO selectivity and formation rate over Cu/ZnO/Al_2O_3 with or without 1.4% NH_3 (reaction conditions: 400 °C, 1 bar, H_2:CO_2:N_2 = 1:1:1, contact time: 0.05 s g mL^{-1}).

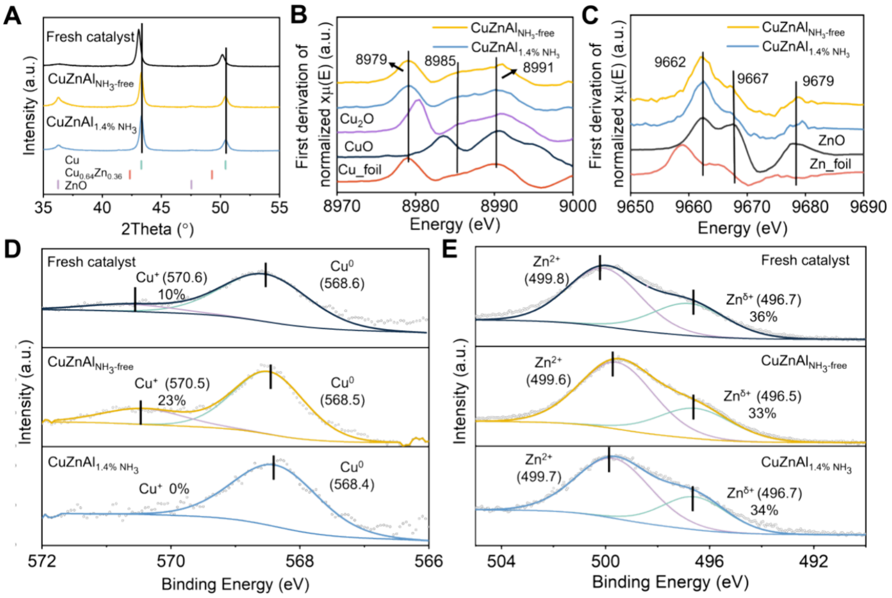

Figure 4. Characterization of fresh and used $Cu/ZnO/Al_2O_3$ catalysts. (A) XRD. (B) Corresponding first derivatives of normalized spectra of Cu K-edge XANES. (C) Corresponding first derivatives of normalized spectra Zn K-edge XANES. (D) Cu LMM Auger spectra. (E) Zn LMM Auger spectra. CuZnAl$_{NH3\text{-free}}$:$Cu/ZnO/Al_2O_3$ exposed to $H_2/CO_2/N_2$ (1:1:1) for 100 h at 400 °C. CuZnAl$_{1.4\%NH3}$:$Cu/ZnO/Al_2O_3$ exposed to $H_2/CO_2/N_2$ (1:1:1) with 1.4% NH_3 for 100 h at 400 °C.

first 15 min and then gradually declined further to 0.6% over 100 h. Notably, after NH_3 addition was halted, the CO_2 conversion recovered to 3.3%, indicating that the deactivation caused by 1.4% NH_3 was largely irreversible after the long-term test. Additionally, CO selectivity gradually decreased, reaching 90.3% over the first 80 h and then rapidly dropping to 54.5% in the subsequent 20 h. This rapid decline in selectivity is attributable to the low formation rate of CO compared to the relatively stable formation rate of CH_4 (Figure S29).

We employed XRD analysis to investigate changes in the bulk phase of the catalyst (Figure 4A and Figure S30). Notably, after 100 h of TOS in the presence of 1.4% NH_3, CuO was not detected in the XRD pattern, indicating the copper oxidation did not contribute to the deactivation mechanism. A slight shift in the diffraction peaks of copper in the fresh catalyst suggested the formation of a CuZn alloy.[45] Rietveld refinement of the XRD data revealed that the lattice parameter of Cu in the fresh catalyst was 3.633 Å, while the lattice parameter in the used catalysts was 3.618 Å, which is close to the standard lattice parameter of metallic Cu (3.615 Å, PDF 01-085-1326) (Figure S31 and Table S3). This suggests that Cu in the catalysts occurred in the metallic form. The expansion of the Cu lattice in the fresh catalyst was attributed to Zn incorporation.[46,47] These results confirm the formation of a CuZn alloy in the fresh catalyst and its disappearance after the reaction. The high Cu/Zn ratio (3.0) determined from XRD refinement of the fresh catalyst, which exceeds the ratio derived from ICP analysis (2.5), further supports the formation of a CuZn alloy (Tables S1 and S3).[46,47] Alloy formation due to Zn doping into the Cu lattice enhanced the diffraction intensity of Cu peaks in the XRD pattern while reducing the intensity of ZnO peaks, resulting in a higher Cu/Zn ratio. Although CuZn alloys are known to form upon hydrogen reduction, their inherent instability during catalytic processes makes them undetectable in postreaction catalysts.[32,45] XRD refinements of the used catalysts revealed a consistent Cu/Zn ratio of 1.8, indicating that NH_3 did not alter the phase or composition of the catalyst. Additionally, the crystallite sizes for Cu and ZnO were measured as 26.6−28.7 nm and 1.5−2.3 nm, respectively, demonstrating resistance to sintering in both the absence and presence of NH_3 (Table S3). This suggests that sintering, which is often reported as a deactivation mechanism during CO_2 hydrogenation, was not a significant issue here.[48,49] H_2 TPD results further confirmed the minimal variation in metal dispersion (Figure S32 and Table S4). Additionally, the addition of 1.4% NH_3 caused only a minor decrease in surface area, from 59 $m^2\ g^{-1}$ (without NH_3) to 54 $m^2\ g^{-1}$ (with 1.4% NH_3) (Table S5).

We subsequently conducted X-ray absorption spectroscopy (XAS) on the used catalysts. The Cu K-edge X-ray absorption near-edge structure (XANES) results after 100 h of TOS with and without 1.4% NH_3 showed negligible differences, with both conditions prominently displaying characteristics of metallic Cu (Figure S33). A detailed analysis of the first derivatives of the Cu K-edge XANES spectra revealed a subtle shoulder at 8985 eV (Figure 4B), indicating minor oxidation of the Cu particles.[50] The Zn K-edge XANES spectra were consistent with those of ZnO, showing a prominent peak at 9662 eV in the first derivative of Zn K-edge XANES (Figure 4C and Figure S34). This peak indicates that the zinc sites retained their oxidation state.[51]

To quantify the valence states of the cations, linear combination fitting (LCF) of the XANES spectra was performed. For Cu species, with XRD data ruling out the presence of the CuO phase and XAS serving as a bulk phase analysis technique, we used standards of Cu foil and Cu_2O. After 100 h of TOS, the proportion of Cu^+ (calculated as $Cu^+/(Cu^0+Cu^+)$) in the catalyst was 33% under NH_3-free conditions and 38% in the presence of 1.4% NH_3, indicating a similar extent of slight oxidation of Cu particles (Figures S35 and S36 and Table S6). Moreover, the proportions of Zn^0 (calculated as $Zn^0/(Zn^0+Zn^{2+})$) were 18 and 19% for the catalysts under NH_3-free and 1.4% NH_3 conditions, respectively. This indicates the formation of ZnO_x species

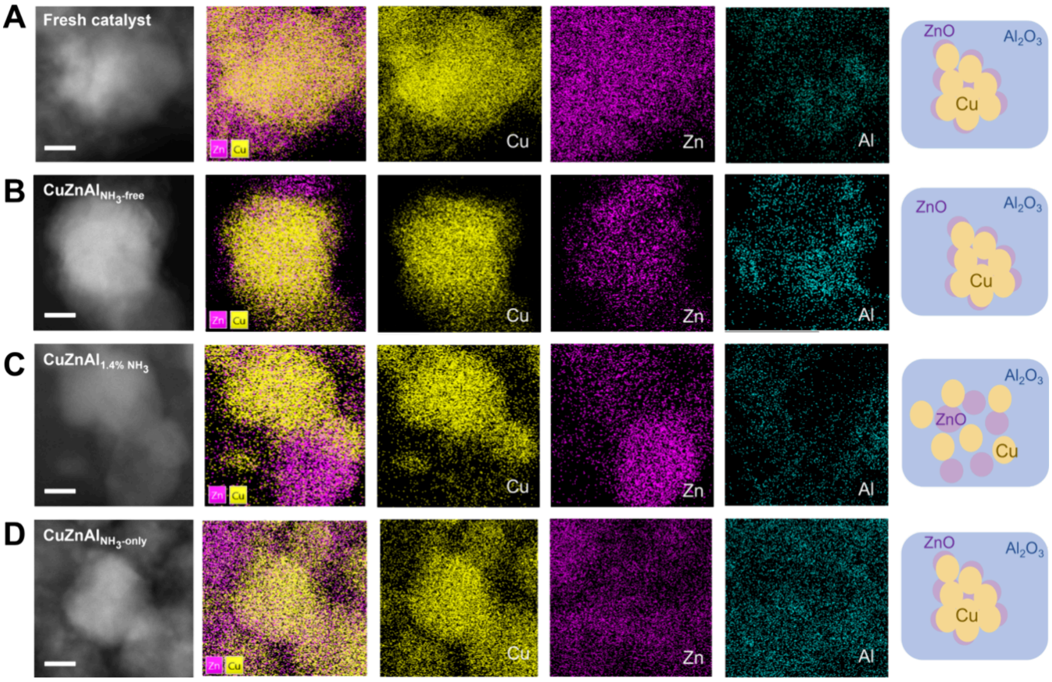

Figure 5. HAADF−STEM analysis and EDX mapping of $Cu/ZnO/Al_2O_3$. (A) Fresh $Cu/ZnO/Al_2O_3$. (B) Catalyst used for 100 h of TOS under NH_3-free conditions, (C) catalyst used for 100 h of TOS in the presence of 1.4% NH_3. (D) Catalyst exposed to 1.4% NH_3/N_2 (in the absence of CO_2 and H_2) for 100 h. Scale bar: 10 nm.

and the presence of $Zn^{\delta+}$ ($0 < \delta < 2$) (Figures S37 and S38 and Table S6). The consistency in the oxidation states of zinc and copper across the used catalysts suggests minimal variability, indicating that NH_3 did not significantly affect the chemical states of these metals.[45]

Extended X-ray absorption fine structure (EXAFS) analysis at the Cu K-edge was conducted to elucidate the local structure and electronic states of copper in the catalysts (Figures S39 and S40). Considering that EXAFS cannot differentiate between Cu−Cu and Cu−Zn scattering paths, the observed path is attributed to Cu−Cu, given the instability of CuZn alloys during the reaction process (vide supra). Both catalysts exhibited a distinct peak at 2.54 Å, corresponding to Cu−Cu scattering, and a weaker peak around 1.90 Å, corresponding to Cu−O scattering. The inverse transforms of these peaks were fitted using parameters for Cu−Cu and Cu−O scattering, respectively (Figures S41 and S44 and Table S7). Both catalysts exhibited the same Cu−Cu distance of 2.54 Å and similar coordination numbers (CNs) of 6.68 (NH_3-free) and 6.29 (1.4% NH_3). Under NH_3-free conditions, the CN for Cu−O was 0.34 at a distance of 1.89 Å, which slightly increased to 0.50 at a similar distance of 1.88 Å in the presence of 1.4% NH_3. These findings indicate mild oxidation of the used catalysts with no pronounced changes in the copper state or structure. Considering that CN can serve as an indicator of crystal size,[52] the reduction in CN from 6.68 to 6.29 for the Cu−Cu path suggests minimal changes in Cu particle size in the presence of NH_3, consistent with the XRD results (Table S3).

In addition, Zn K-edge EXAFS analysis revealed Zn−O and Zn−Zn scattering paths, similar to those observed in standard ZnO (Figures S45 and S46). The inverse transforms of the peaks were fitted using Zn−O and Zn−Zn scattering parameters at distances of 1.97 and 3.21 Å, respectively (Figures S47−S50). The CN for the Zn−O path showed a minor increase from 0.61 at 1.95 Å under NH_3-free conditions to 0.74 at 1.96 Å with a 1.4% NH_3 exposure. Conversely, the CN for the Zn−Zn path slightly decreased from 1.81 at 3.21 Å (NH_3-free) to 1.23 at 3.23 Å (1.4% NH_3) (Table S7). The Zn K-edge EXAFS analysis results, under both NH_3-free and 1.4% NH_3 conditions, suggest consistent Zn−O CNs, indicating that zinc remained in its oxidized state throughout the experiment. Additionally, the size of the ZnO structures, likely nanoparticles, showed no significant changes, consistent with the XRD results (Table S3). Consequently, these findings imply that exposure to NH_3 did not significantly affect the electronic or structural states of zinc or copper in the catalysts. Further analysis is required to fully understand the impact of NH_3 on the catalysts (vide infra).

We then employed X-ray photoelectron spectroscopy (XPS) to elucidate the elemental states of the surface of the catalysts. The samples were carefully transferred in an airtight holder to prevent exposure to air. The XPS spectra of the O 1s revealed distinct peaks at 531.9 and 533.3 eV, corresponding to lattice oxygen (O_L) and oxygen vacancies or defects (O_V), respectively (Figure S51 and Table S8). The $O_V/(O_V+O_L)$ ratio indicated that the quantity of surface defect due to the formation of ZnO_x[53] remained unchanged. This suggests a consistent ZnO_x content, consistent with the XANES findings. Defects have been reported to promote the formation of ZnO_x, which stabilizes a ZnO_x overlayer on the Cu surface and acts as a cocatalyst in CO_2 hydrogenation.[54,55] During the CO_2 hydrogenation to methanol process, the oxygen-vacant ZnO_{1-x}/Cu interface, rather than Cu alone, CuZn alloy, and stoichiometric oxygen fully terminated ZnO/Cu interfaces, exhibits much higher intrinsic activity for methanol production.[56,57] Furthermore, studies have proposed that $Cu-ZnO_x$, rather than the CuZn alloy, mainly drives the catalytic activity,[58−60] a notion supported by the unstable nature of the CuZn alloy under CO_2 hydrogenation conditions.[45]

Cu 2p XPS, supported by XRD and XANES, confirmed the absence of Cu^{2+}species in all samples (Figure S52). To further evaluate the state of Cu after CO_2 hydrogenation, Auger electron spectroscopy, which is highly sensitive to distinguishing between Cu^0 and Cu^+ states, was employed (Figure 4D).[61] Analysis of the Cu LMM Auger region revealed that the fresh catalyst contained 10% Cu^+ sites, while the used catalyst under NH_3-free conditions had 23% Cu^+ sites (Table S9). Notably, in the Cu LMM Auger spectrum of the catalyst used under 1.4% NH_3 conditions, no Cu^+ sites were detected, indicating that only metallic Cu was present on the catalyst surface (vide infra). Furthermore, the Zn 2p core-level and LMM Auger electron spectra of the used catalysts (Figure 4E, Figure S53, and Table S10) were consistent with those of the fresh catalysts, indicating the predominant presence of oxidized states.[62] All catalysts exhibited similar proportions of $Zn^{\delta+}$, corroborating the presence of ZnO_x and suggesting the absence of significant changes in the ZnO phase, consistent with the XANES results.

High-angle annular dark-field−scanning transmission electron microscopy (HAADF-STEM) combined with energy-dispersive X-ray (EDX) spectroscopy was employed to elucidate the structural attributes of the catalysts. First, the fresh $Cu/ZnO/Al_2O_3$ catalyst exhibited a uniform dispersion of Cu and Zn (Figure 5A). EDX analysis after 10 h of TOS, both with and without NH_3, revealed no substantial differences compared with the fresh catalyst (Figure S54). However, at a prolonged TOS of 100 h, the catalyst used under NH_3-free conditions continued to show a uniform distribution of Cu and Zn (Figure 5B). In contrast, the catalyst exposed to 1.4% NH_3 displayed a noticeable separation between Cu and ZnO (Figure 5C and Figure S55). When the catalyst was exposed solely to NH_3 (without CO_2 and H_2) for 100 h, this separation was not observed (Figure 5D). This separation is crucial for understanding the catalytic mechanisms in the RWGS reaction, as the Cu−ZnO_x interface plays a pivotal role.[59,63,64] Hydrogen is weakly chemisorbed on metallic Cu, as Cu is known to quickly dissociate and recombine with hydrogen.[65] The dissociated H is transferred to ZnO_x, where it reacts with carbonates. Therefore, the separation of Cu and ZnO complicates the reaction between the dissociated hydrogen and carbonates. Cu−ZnO_x interfaces accelerate reaction rates compared with surfaces with only Cu.[54,60,66−68] Reaction rates on Cu surfaces with deposited ZnO nanoparticles can be 5 to 18 times higher than those on the most reactive Cu surfaces.[60] Additionally, intermediates involved in methanol formation undergo faster hydrogenation owing to the interaction between Cu and Zn, compared with reactions occurring solely on Cu surfaces.[45]

According to our earlier observations, NH_3 exhibited a pronounced affinity for adsorption at the $Zn^{\delta+}$ sites at the Cu−ZnO_x interface. This interaction weakened the bonding between Cu and O from ZnO_x, leading to an elongation of the Cu−O bond. Consequently, the binding energy at the interface between ZnO_x and Cu decreased, shifting the valence state of Cu toward a more neutral (zero) state, as confirmed via XPS analysis. This reduction in the binding energy between Cu and ZnO_x suggests a fundamental mechanistic pathway for the observed detachment phenomena. Moreover, H_2 temperature-programmed reduction (H_2 TPR) results indicated a significant decrease in H_2 consumption under the 1.4% NH_3 condition (Figure S56 and Table S11), suggesting a reduction in Cu^+ sites, which aligns with the observed separation of Cu and ZnO. Additional evidence from thermodynamic calculations showed that the reaction between Cu_2O and NH_3 had a significantly lower Gibbs free energy compared with the reaction between Cu_2O and H_2 at temperatures above 200 °C (Figure S57). This finding suggests that NH_3 enhanced the tendency to prolong Cu−O bonds, leading to the formation of Cu^0 sites. This was particularly evident in cases where NH_3 had a stronger adsorption affinity to the catalyst surface compared with H_2 (−1.11 eV of NH_3 at the Cu−ZnO_x interface and −0.72 eV of NH_3 on the Cu surface, compared with −0.06 eV of H_2 on the Cu surface, Figure S22 and Table S2). It should be noted that the conversion from Cu^+ to Cu^0 sites was observed only on the surface and not in the bulk phase. XANES and XRD analyses, which were employed to investigate changes in the bulk phases of Cu and Zn, showed no substantial transformations.

We conducted an operando DRIFTS experiment for 100 h of TOS to elucidate the evolution of reaction intermediates (Figures S58 and S59). Spectroscopic analysis revealed a significant shift in the band from 2203 to 2210 cm^{-1} during the reaction, which was attributed to the *NCO species. This shift was correlated with a rapid decline in activity at the initial stage and gradual deactivation over the long-term test, as quantified via GC (Figure S58). Notably, the *NCO species adsorbed on the ZnO surface was identified at 2210 cm^{-1} (Figure S25). This shift suggests a gradual transformation of the adsorption sites from the Cu−ZnO_x interface to the ZnO surface. Additionally, the initially subtle band at 1448 cm^{-1} became more pronounced as the reaction progressed, indicating increased NH_3 adsorption. This change highlights a rise in the NH_3 adsorption intensity on both ZnO and Cu surfaces (Figures S20 and S59).

Subsequent CO_2 adsorption experiments were conducted on the used catalyst (Figure S60), which had undergone a 100 h test in a $CO_2/H_2/N_2$ (1:1:1) stream with 1.4% NH_3. A notable shift in the adsorption band from 1538 cm^{-1} (carbonate on the Cu−ZnO_x interface) to 1528 cm^{-1} (carbonate on the Cu surface) occurred, indicating the separation of ZnO from Cu.[69] Additionally, the increased intensity of bands at 1335 cm^{-1} (carbonate on the ZnO surface) confirmed the increased presence of these species on the ZnO surface,[21,70] as supported by direct CO_2 adsorption on ZnO samples (Figure S21). Moreover, a semiquantitative comparison of the intensity of carbonate bands revealed a marked decrease in signal intensity at the Cu−ZnO_x interface (Figure S60), indicating a reduction in the exposed Cu−ZnO_x interface owing to the separation of Cu and ZnO. Prior to the reaction, weak signals from carbonate on ZnO were present but were overshadowed by the stronger signals from the Cu−ZnO_x interface. After the reaction, as the carbonate signals at the Cu−ZnO_x interface decreased, the signals from the ZnO surface became more pronounced.

DFT-Computed Changes in Reaction Pathways due to NH_3 Addition

The effect of NH_3 on the reaction was calculated by using DFT. The computational model featured a Cu(111) surface loaded with ZnO particles. First, the adsorption of NH_3 on the active sites was evaluated. The results revealed lower adsorption energy for NH_3 (−1.11 eV at the Cu−ZnO_x interface) compared with that of CO_2 (−1.00 eV at the Cu−ZnO_x interface), CO (−0.95 eV on the Cu surface), and H_2 (−0.06 eV on the Cu surface) (Figure S22 and Table S2). This

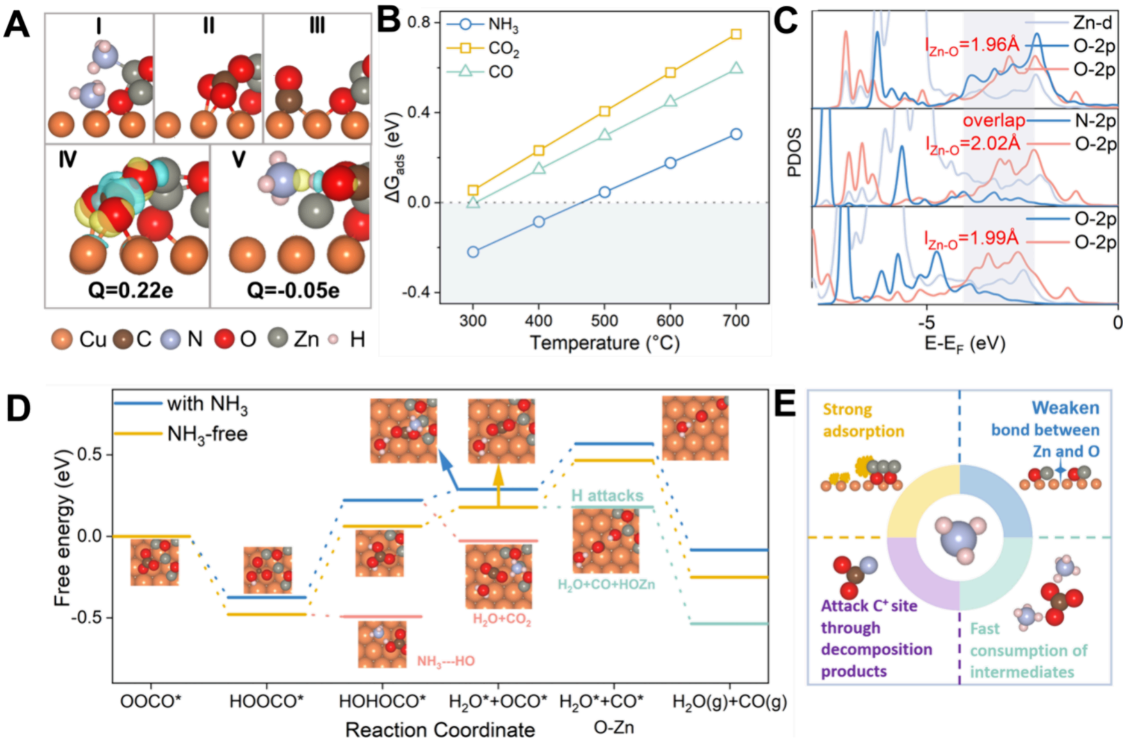

Figure 6. DFT calculation of NH_3 effects on the reaction. (A) Adsorption configuration of the reaction gas (I–III) and charge density difference diagrams for CO_2 adsorption and NH_3–HO structure (IV and V; blue represents electron dissipation, yellow represents electron accumulation; isosurface value: 0.005 e bohr^{-3}). (B) Adsorption free energy of the reaction gases at the Cu–ZnO_x interface. (C) Projected density of states with and without NH_3 adsorption and with H_2O adsorption. (D) Free energy of the reaction at the Cu–ZnO_x interface. (E) Summary of the effect of NH_3 on the reaction.

favorable adsorption of NH_3 facilitated its occupation of the reaction sites (Figure 6A I–III). The temperature-dependent adsorption free energy diagram obtained from calculations revealed that as the temperature increased, the adsorption free energies of NH_3, CO_2, and CO on the Cu–ZnO_x interface also increased. This suggests a decreased adsorption capacity at the Cu–ZnO_x interface, indicating a weakened inhibitory effect (Figure 6B and Figures S3 and S61). For reactions on the Cu(111) surface, the formation of HCOO* (with an energy change of −0.75 eV) was found to be more favorable than the formation of *COOH (with an energy change of 0.04 eV). Conversely, at the Cu–ZnO_x interface, HCO_3* emerged as the favorable intermediate with a lower reaction energy of −0.91 eV (Figure S62). Additionally, HCOO* is more likely to be an intermediate in CH_4 production,[38,71] which further supports the observation that CH_4 generation from the Cu(111) surface remained unaffected, while CO formation was suppressed at the Cu–ZnO_x interface.

The CO_2 configuration with the lowest adsorption energy at the interface was further examined, and the results revealed the formation of a CO_3* intermediate. The adsorption of NH_3 will affect the interaction between the CO_3* intermediate and the interface, which is reflected in the weakening of the Zn–O bond. The charge density difference diagram of CO_2 at the interface after NH_3 adsorption indicates that CO_2 acquires electrons from both ZnO and Cu, leading to elongation in the Zn–O bond (Figure 6A IV and Figure S63). NH_3, through its lone pair of electrons, influenced the distribution of Zn d orbitals, leading to increased Zn–N overlap peaks below the Fermi level and causing Zn–O bond stretching. This interaction facilitated the separation of O from Zn, a process that cannot be achieved with bulk O atoms or O in H_2O, which also contains lone-pair electrons (Figure 6C and Figure S64). Moreover, during the hydrogenation process, hydrogenation of the O atom at the edge of the CO_3* intermediate was identified as the most favorable pathway (Figure S65). The hydrogenation led to detachment of the O atom from the edge and the Cu surface. Additionally, NH_3 adsorption on the Cu surface did not affect the transition-state energy of the hydrogenation process, which remained approximately 0.42 eV in both scenarios (Figure S66).

The reaction free energy profile at the Cu–ZnO_x interface is depicted in Figure 6D. For the initial hydrogenation step, the energy change at the interface was −0.48 eV without NH_3 adsorption, which is more negative than the value in the presence of NH_3 (−0.37 eV). This indicates that NH_3 decreases the tendency for the hydrogenation reaction. In the subsequent step involving H_2O generation, hydrogenation on the pre-existing −OH structure showed a higher energy barrier (>1.05 eV). Consequently, it is more probable that hydrogenation would proceed on another oxygen atom of the CO_2 molecule, accompanied by hydrogen transfer to regenerate H_2O with an energy change of <0.60 eV. However, the presence of NH_3 hindered the process of hydrogen transfer due to structural variations induced by hydrogenation on the −OH structure compared to when NH_3 was absent (Figure S67). NH_3 induced the separation of the O atom with a free energy change of −0.25 eV, thereby hindering CO formation and increasing the formation energy barrier of HOHOCO* from 0.54 to 0.60 eV. Additionally, NH_3 adsorption enhanced the interaction between N and Zn, which increased the distance between Zn and Cu (Figure 6C and Figure S63). This

https://doi.org/10.1021/jacsau.4c01097
JACS Au 2025, 5, 1243−1257

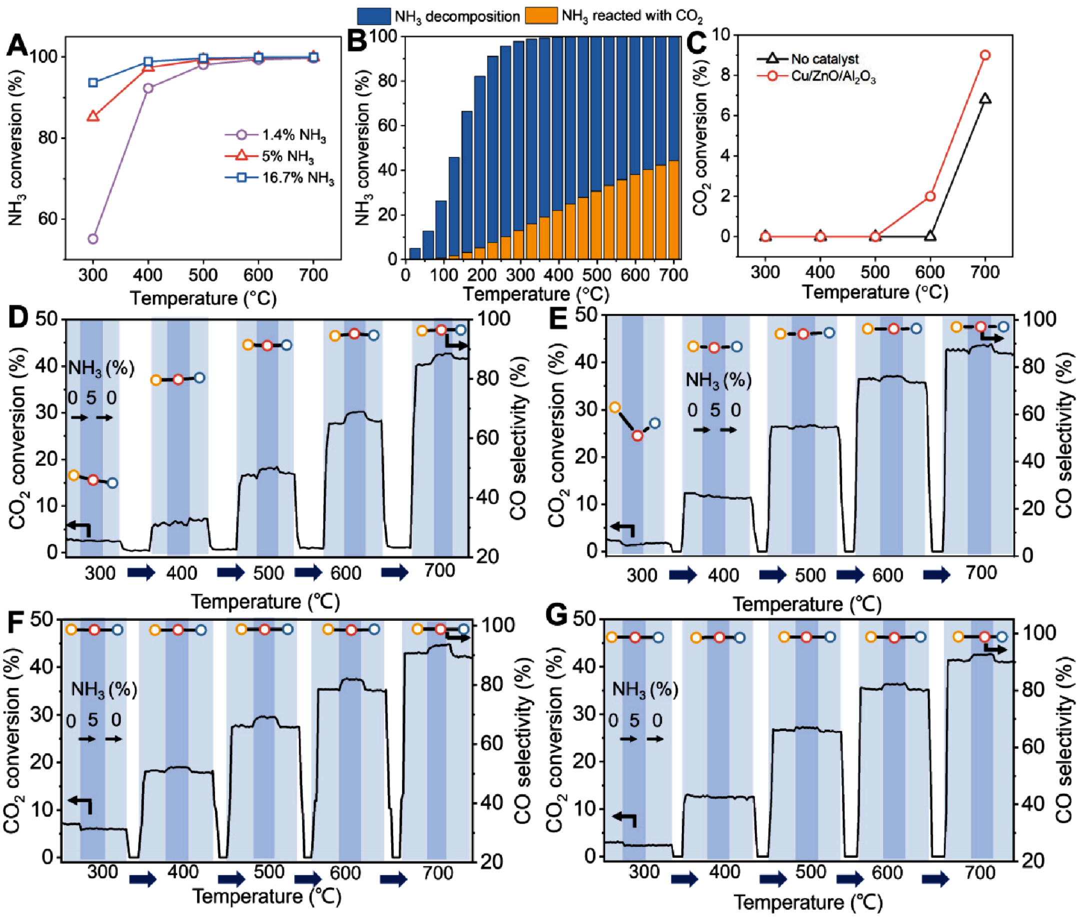

Figure 7. Design of the NH_3-tolerant catalyst in RWGS. (A) NH_3 conversion calculated from the thermodynamic equilibrium of CO_2 hydrogenation under different NH_3 concentrations. (B) NH_3 conversion calculated from the thermodynamic equilibrium of the reaction between CO_2 and NH_3 (CO_2:NH_3 = 3:2, 1 bar, Gibbs reactor). (C) Experimental results of the reaction between CO_2 and NH_3 (1 bar, CO_2:N_2 = 1:2, 5% NH_3, contact time: 0.05 s g mL^{-1}). Role of 5% NH_3 on NH_3-tolerant catalysts in the hydrogenation of CO_2 over (D) Ru−Cu/ZnO/Al_2O_3, (E) Ni−Cu/ZnO/Al_2O_3, (F) β-Mo_2C, and (G) Pt/TiO_2 (reaction conditions: H_2:CO_2:N_2 = 1:1:1, contact time: 0.05 s g mL^{-1}).

increased distance made it more difficult for the COO* intermediate to be stabilized without being anchored by adjacent Zn atoms (Figure S68). Thus, the reaction tended to proceed with the detachment of bulk O, leading to CO_2 production. In the absence of NH_3, the formation of a CO−O−Zn intermediate (COO*) resulted in CO production.

Hydrogenation can occur in different directions on the O atom, leading to the adsorption of generated H_2O on the Zn surface. However, detachment of the O atom would still occur. Additionally, CO_2 adsorbed at the edge Zn site can be hydrogenated in two steps to produce CO. Unfortunately, NH_3 often showed a higher affinity for occupying this Zn site (Figure S69). Analysis of charge density difference diagrams and electron transfer numbers indicated that the degree of anchoring between Cu and ZnO decreased in the presence of NH_3, leading to an increased dispersion potential (Figure S70). This observation is consistent with the experimentally observed separation between Cu and ZnO. Once Cu and ZnO are separated, it becomes difficult to re-establish the Cu-ZnO_x interface. After the separation, the adsorption free energy of CO_2 at the Zn−Cu interface increases, suggesting that this site is unsuitable for CO_2 to undergo further reaction, that is, oxygen remains at the Zn site, allowing the Zn−O−Cu structure to reform and be reduced to CO (Figure S71). In this case, CO_2 is more likely to react at the Zn site on the ZnO edge, producing CO.

Note that when the catalyst was exposed solely to NH_3 (without CO_2 and H_2), the separation of Cu and ZnO did not occur (Figures S22 and S72). When NH_3 adsorbs at the $Zn^{\delta+}$ site, the Zn−O−Cu structure remains intact, suggesting that the interface is not disturbed. The distance between Zn and the nearest Cu atom is 3.41 Å. Upon CO_2 adsorption at the interface, the O−Cu bond in the Zn−O−Cu structure is significantly weakened or even broken. Oxygen bonds with the carbon atom of CO_2, forming a Zn−O−C structure, and the distance between Zn and Cu increases to 4.18 Å. Moreover, during this process, NH_3 adsorption elongates the Zn−O bond, weakening the orbital overlap of Zn−O (Figure 6C), which creates favorable conditions for the subsequent cleavage of the Zn−O bond. As a result, the increased distances between Zn−O and Zn−Cu facilitate catalyst separation.

Furthermore, NH_3 and the −OH structures within HCO_3* species generated during the reaction exhibited significant electron transfer effects (Figure 6A V), indicating the possibility of a potential chemical reaction between NH_3 and the −OH groups. In comparison to the hydrogenation reaction with a higher energy barrier, the NH_3 adsorption process only showed a significantly lower energy change of −0.01 eV, making it more favorable for occurrence. This favorable energy change resulted in the formation of NH_4 structures and accelerated the conversion of intermediate HCO_3 into ammonium bicarbonate or ammonium carbonate, as supported by experimental results (Figure 6D,E, and Figure S73). Moreover, the catalyst interface lowered the energy barrier for decomposition of NH_3 into NH_x and H, allowing decomposition at temperatures below 700 °C (Figure S74). NH_x structures adsorbed on the Cu surface can potentially attack the C^+ site, possibly leading to the formation of *NCO structures (Figure 6E and Figure S75). Intergrated crystal orbital Hamilton population (ICOHP) analysis indicated that the N−C bonding in *NCO was excessively strong, which inhibited the CO desorption (Figure S76).

Design of the NH_3-Tolerant Catalyst in RWGS

According to the thermodynamic equilibrium calculations for CO_2 hydrogenation in the presence of NH_3 (Figure 7A and Figure S77), CO_2 conversion considerably increased with higher NH_3 concentrations, suggesting that NH_3 participated in the RWGS reaction to produce CO, H_2O, and N_2. Thermodynamic equilibrium calculations indicated that NH_3 underwent nearly complete decomposition into N_2 and H_2, leaving minimal residual NH_3 (Figure 7A). A stream with either 5 or 100% NH_3 alone resulted in nearly complete NH_3 decomposition starting at 300 °C (Figure S78). In our RWGS experiments, extending the contact time at 400 °C, which promoted the reaction toward equilibrium, effectively suppressed the detrimental effects of NH_3 (Figure S10). Conversely, increasing the H_2/CO_2 ratio suppressed NH_3 decomposition because the higher H_2 concentration inhibited NH_3 decomposition, in accordance with Le Chatelier's principle. This, in turn, potentially enhanced the role of NH_3 in inhibiting the RWGS reaction (Figure S11).

Furthermore, thermodynamic equilibrium calculations for the NH_3-CO_2 reaction, conducted at various theoretical NH_3/CO_2 ratios, showed an enhancement in CO_2 conversion to CO with increasing temperatures (Figure 7B and Figure S79). NH_3 was completely decomposed above 350 °C, resulting in the formation of N_2 and H_2. Additionally, we experimentally investigated the direct interaction between CO_2 and NH_3. The results demonstrated that CO_2 could react with NH_3 at 700 °C even without a catalyst (Figure 6C and Figures S80 and S81). This phenomenon was further confirmed by DRIFTS experiments (Figure S14). When employing the $Cu/ZnO/Al_2O_3$ catalyst, the reaction between CO_2 and NH_3 commenced at 600 °C, elucidating why higher temperatures mitigate the inhibitory effect of NH_3 (Figure 1C,D and Figure S3).

To mitigate the adverse effects of NH_3, we modified the catalysts to facilitate NH_3 decomposition. Considering that Ru and Ni have been reported as efficient catalysts for NH_3 decomposition,[72,73] we synthesized catalysts with Ru (5%) or Ni (5%) loaded on $Cu/ZnO/Al_2O_3$ through the impregnation method. The modified catalysts showed high resistance to a high concentration (5%) of NH_3 (Figure 7D,E). Notably, both Ru and Ni demonstrated catalytic activity in CO_2 methanation, even at low temperatures (300−400 °C).[74,75] Therefore, the Ni/Ru-modified catalysts exhibited lower CO selectivity than the unmodified $Cu/ZnO/Al_2O_3$, which exhibited high CO selectivity (≥90% at 300−700 °C).

Studies have reported that β-Mo_2C and Ni/CeO_2 are effective catalysts for NH_3 decomposition.[76,77] Another study suggested that the NH_3 decomposition rates for transition metals followed the order Ru > Ni > Pt > Pd.[73] Consequently, we synthesized and evaluated the performance of β-Mo_2C, Ni/CeO_2, Pt/TiO_2, and Pd/Al_2O_3 (Figure 7F,G and Figure S82), all of which are recognized for their effectiveness in CO_2 hydrogenation.[3] Among the catalysts, β-Mo_2C, Ni/CeO_2, and Pt/TiO_2 exhibited notable resistance to NH_3 during the CO_2 hydrogenation. Specifically, β-Mo_2C maintained a stable performance even at 5% NH_3 concentration (Figure 7F). At 300 °C, only a slight activity loss occurred, with conversion decreasing from 7.1 to 6.1%, owing to the low NH_3 decomposition activity at this temperature. From 400 to 700 °C, CO_2 conversion slightly increased under 5% NH_3 condition, attributed to the reaction between CO_2 and NH_3 (or NH_3-derived H_2), while CO selectivity remained at 100% across this temperature range of 300−700 °C. Similarly, Pt/TiO_2 and Ni/CeO_2 demonstrated excellent NH_3 resistance, showing only minimal activity loss at 300 °C (Figure 7G and Figure S82). At temperatures above 500 °C, a slight increase in the level of CO_2 conversion was observed. In contrast, Pd/Al_2O_3 showed relatively low activity in the presence of 5% NH_3, with a noticeable reduction in activity across the 300−600 °C temperature range. This decrease was due to the lower NH_3 decomposition rate of Pd compared to those of the other metals such as Ru, Ni, and Pt.

■ DISCUSSION

This work elucidates the impact of NH_3 on industrial $Cu/ZnO/Al_2O_3$ catalysts during the RWGS reaction. In short-term tests, NH_3 acts as a reversible poison by competing for adsorption on the catalyst surface and hindering the hydrogenation of carbonate, thereby reducing the catalyst activity. In contrast, during prolonged CO_2 hydrogenation reactions over 100 h, NH_3 works as an irreversible poison. As a result, the interaction of NH_3 with the catalyst surface triggers the separation of Cu and ZnO attributed to the loss of Cu^+ sites on the surface, resulting in a gradual decline in the overall catalytic performance and eventual complete deactivation. Notably, we alleviate the adverse effects of NH_3 on $Cu/ZnO/Al_2O_3$ by catalytically decomposing NH_3 into N_2 and H_2. This finding lays the foundation for the rational design of a group of inherently NH_3-resistant catalysts.

■ METHODS

Catalyst Synthesis

The industrial $Cu/ZnO/Al_2O_3$ catalyst was purchased from Tianjin Kaite New Material Technology Co., Ltd. The concentrations of Cu, Zn, and Al in the catalysts were determined via ICP-OES (iCAP 7400, Thermo Fisher; Table S1).

The 5% $Ni-Cu/ZnO/Al_2O_3$ catalyst was synthesized through a wet impregnation method. First, 25 mg of nickel nitrate hexahydrate ($Ni(NO_3)_2\cdot 6H_2O$, 99.99%, Aladdin Co., Ltd.) was dissolved in 10 mL of deionized water. This solution was then added dropwise to a suspension of $Cu/ZnO/Al_2O_3$ in 100 mL of deionized water. The resulting mixture was continuously stirred and dried at 80 °C overnight. The obtained catalyst was then reduced at 500 °C for 2 h (heating rate of 10 °C min^{-1}) under a 5% H_2/N_2 atmosphere prior to use. The same synthesis protocol was employed to prepare the 5% $Ru-Cu/ZnO/Al_2O_3$ catalyst, with 3 mL of ruthenium nitrosyl nitrate ($Ru(NO)(NO_3)_x(OH)_y$, $x+y = 3$, 0.15 g L^{-1} Ru, supplied by Aladdin Co., Ltd.) replacing the nickel nitrate hexahydrate.

The 5% Pd/Al_2O_3 catalyst was synthesized through the incipient wetness impregnation method.[78] γ-Al_2O_3 powder (surface area of 200 $m^2\ g^{-1}$) and $Pd(NH_3)_4(NO_3)_2$ (purity of 98%) were purchased from Aladdin Co., Ltd. After impregnation, the catalysts were dried at 100

°C overnight. The dried catalyst was then calcined at 500 °C for 2 h (heating rate of 10 °C min^{-1}) in a 6.7% O_2/N_2 atmosphere and subsequently reduced at 500 °C for 30 min (heating rate of 10 °C min^{-1}) under a 2% H_2/N_2 atmosphere.

The CeO_2 nanorod was synthesized through a modified reported method.[79] First, $Ce(NO_3)\cdot 6H_2O$ (4.8 g, Sigma-Aldrich Co., Ltd., 99.999%) was dissolved in 10 mL of deionized water, and then the resulting solution was added to a NaOH solution (Greagent, ≥96%). The mixture was stirred for 1 h and then diluted with 140 mL of water. The resulting solution was transferred to a stainless-steel autoclave (300 mL) and maintained at 100 °C for 24 h. The obtained solid was centrifuged, rinsed, and then calcined at 700 °C to yield CeO_2 nanorods. 5% Ni/CeO_2 was prepared through a wet impregnation method using $Ni(NO_3)_2\cdot 6H_2O$ (analytical reagent) as the precursor. After impregnation, the solid was calcined at 700 °C for 2 h (heating rate of 10 °C min^{-1}) and then reduced at 500 °C for 2 h (heating rate of 10 °C min^{-1}).

Similarly, the 1% Pt/TiO_2 catalyst was prepared through a wet impregnation method with $PtCl_4$ and TiO_2 (both from Aladdin Co., Ltd.). The resulting solid was first reduced in 30% H_2/N_2 at 300 °C for 3 h (heating rate of 10 °C min^{-1}) to remove chloride. The solid was then calcined in air at 400 °C for 4 h (heating rate of 10 °C min^{-1}). Prior to testing, the catalyst was pretreated in a H_2 flow at 500 °C for 2 h (heating rate of 10 °C min^{-1}).

Mo_2C was synthesized via a temperature-programmed carburization procedure.[80] First, $(NH_4)_6Mo_7O_{24}\cdot 4H_2O$ (Aladdin Co., Ltd.) was heated in a muffle furnace to 500 °C at a rate of 10 °C min^{-1} and held at this temperature for 4 h to prepare the MoO_3 precursor. The material was then crushed and sieved to a particle size of 300−450 μm. To obtain β-Mo_2C, the powder was carburized in a tubular quartz reactor under a 20% CH_4/H_2 (150 mL min^{-1}) flow. The temperature was ramped from room temperature to 300 °C at 5 °C min^{-1}, and then from 300 to 700 °C at 1 °C min^{-1}, and held at 700 °C for 2 h. The resulting material was cooled to room temperature under a N_2 flow and then passivated with 1% O_2/N_2 for 12 h. Before testing, Mo_2C was pretreated in 15% CH_4/H_2 at 590 °C for 2 h with a heating rate of 10 °C min^{-1}.

Catalyst Characterization

N_2 physisorption isotherms were measured by using an Autosorb iQ Station 2 apparatus at −196 °C. The materials were first degassed at 300 °C under N_2 flow overnight. The Brunner−Emmet−Teller surface area was determined according to the International Union of Pure and Applied Chemistry.[81] Barrett−Joyner−Halenda analysis was applied to obtain pore size distributions. The carbon black model or the Harkins−Jura statistical thickness model was used for the calculation.

TEM and STEM coupled with EDX spectroscopy were performed by using a high-resolution field emission transmission electron microscope (JEM-2100F), which featured advanced drift correction capabilities. The microscope was operated at an electron acceleration energy of 200 kV, achieving a point resolution of 0.23 nm and a STEM resolution of 0.20 nm. The lattice resolution was 0.10 nm, allowing for precise energy spectrum element analysis over a broad range from beryllium (Be, atomic number 4) to uranium (U, atomic number 92). Molybdenum grids were used instead of Cu grids to avoid interference from the Cu scattering.

Powder XRD data were collected using a Bruker D8 Advance diffractometer equipped with a Bragg−Brentano high-definition mirror, operated at 60 kV and 300 mA with Cu Kα radiation (λ = 1.5406 Å). The materials were scanned over a 2θ range of 5−90° with a step size of 0.02° and a scan time of 3 s per step.

XPS was conducted on an ESCALAB Xi^+ instrument (Thermo Fisher Scientific) within an ultrahigh vacuum chamber ($<1.0 \times 10^{-9}$ mbar). A monochromatic Al target and magnetic lens mode were used with an X-ray beam spot size of 500 μm. The pass energy for the survey spectrum was set to 160 eV with a step size of 1.0 eV. For the narrow scan spectrum, the pass energy was 20 eV, and the step size was 0.05 eV. An airtight cell was utilized to transfer samples (mounted on carbon tapes) from the glovebox to the XPS chamber without exposure to air.

H_2 TPR, NH_3 TPD, and H_2 TPD were conducted by using a Micromeritics AutoChem 2920 instrument equipped with a thermal conductivity detector. Approximately 100 mg of the sample was placed in a U-shaped quartz reactor. Prior to the experiments, the sample was dried in an Ar flow at 300 °C for 30 min at a heating rate of 10 °C min^{-1}. H_2 TPR was performed under 5% H_2/Ar from room temperature to 500 °C at a heating rate of 10 °C min^{-1}. For the NH_3TPD experiment, the sample was pretreated at 500 °C under 5% H_2 for 2 h, and then exposed to a 5% NH_3/Ar flow for 30 min at 50 °C, and purged with Ar for an additional 30 min. Subsequently, the sample was heated to 800 °C at a rate of 10 °C min^{-1} under an Ar flow, and the desorbed NH_3 was monitored with the thermal conductivity detector. A control experiment conducted without introduction of NH_3 was performed to establish the background. H_2TPD was conducted using a similar procedure, starting at −50 °C.

DRIFTS measurements were performed by using a Fourier-transform infrared spectrometer (Nicolet 6700) equipped with a mercury cadmium telluride detector. In situ DRIFT spectra were recorded through the collection of 32 scans at a resolution of 4 cm^{-1}. Prior to measurement, the catalysts were pretreated in situ with a flow of 30 mL min^{-1} of 5% H_2 at 500 °C for 2 h. Background spectra were recorded at the corresponding temperatures under a N_2 flow. Subsequently, the catalysts were exposed to a gas flow with the specified composition at a consistent flow rate of 30 mL min^{-1} at the required temperature. For NH_3 adsorption, the reduced sample was exposed to a 1.4% NH_3/N_2 flow (30 mL min^{-1}) for 20 min at room temperature. The NH_3 flow was then stopped, and N_2 was purged for 60 min. The temperature was subsequently increased to 200, 300, and 400 °C at a heating rate of 10 °C min^{-1}, with the corresponding spectra collected at each temperature. For CO adsorption, the in situ-reduced sample was exposed to a 5% CO/N_2 flow (30 mL min^{-1}) for 20 min at room temperature. Subsequently, the CO flow was stopped and N_2 was purged for 60 min. The temperature was then increased to 100, 200, 300, and 400 °C at a heating rate of 10 °C min^{-1}, with spectra collected at each temperature.

Solid-state NMR experiments were conducted by using a JEOL 600 MHz JNM-ECZ600R spectrometer equipped with a 3.2 mm MAS triple resonance probe and employing the single-pulse method. The MAS frequency was set to 12 kHz, and cross-polarization ($^1H-^{13}C$) was utilized as the primary technique, with a ^1H excitation frequency of 100 kHz. For $^1H-^{13}C$ HETCOR experiments, a contact time of 0.5 ms was used, and DUMBO homonuclear ($^1H-^1H$) decoupling was applied during the t_1 period. DD-MAS NMR experiments were also performed.

XAS data for the Cu K-edge and Zn K-edge were collected in the transmission mode using a TableXAFS-500A instrument (Specreation Instruments Co., Ltd.). The electron beam energy was set to 20 keV (top-up), with an energy resolution ranging from 0.5 to 1.5 eV. The samples were ground and pressed into tablets with a diameter of 13 mm. Air-sensitive catalyst samples were sealed in capillaries within a glovebox and analyzed without exposure to air. Cu XAS spectra were obtained at the K-edge in transmission mode using a silicon drift detector, with continuous scanning from 8879 to 9429 eV. Zn XAS spectra were collected at the K-edge in transmission mode using a silicon drift detector, with continuous scanning between 9469 and 10019 eV. The data were processed with Athena software (version 0.9.26),[82] and EXAFS fittings were performed using Artemis software (version 0.9.26).[82]

CO_2 Hydrogenation Reaction

The CO_2 hydrogenation reactions were conducted in a tubular fixed-bed reactor (ID = 6 mm) with 0.05 g of catalyst loaded in the isothermal zone (Figure S1). Prior to each test, the $Cu/ZnO/Al_2O_3$ catalyst was reduced at 500 °C for 2 h (heating rate of 10 °C min^{-1}) under a 5% H_2/N_2 flow (60 mL min^{-1}). The reaction was conducted with gas mixtures of H_2 and CO_2 in ratios of 1:1, 2:1, or 3:1, with N_2 as the balancing gas (1/3). The products were analyzed online using a Gasboard-3100 gas analyzer (Hubei Ruiyi Co., Ltd.). Different contact times were achieved through variation of the gas flow rate from 15 to 60 mL min^{-1}. The product formation rate, CO_2 conversion, and selectivity to each product were calculated using eqs 1−5:

$$N_{x,\mathrm{out}}[\mathrm{molh}^{-1}] = \frac{C_{x,\mathrm{out}} \times N_{N_2,\mathrm{in}}}{C_{N_2,\mathrm{out}}} \quad (1)$$

$$r_x[\mathrm{mmolh}^{-1}\mathrm{g}_{\mathrm{cat}}^{-1}] = \frac{N_{x,\mathrm{out}}}{m_{\mathrm{cat}}} \quad (2)$$

$$X_{CO_2} = \frac{\sum_{i=1}^{n} N_{x,\mathrm{out}}}{N_{CO_2,\mathrm{in}}} \quad (3)$$

$$S_x = \frac{N_{x,\mathrm{out}}}{\sum_{i=1}^{n} N_{x,\mathrm{out}}} \quad (4)$$

$$t = \frac{m_{\mathrm{cat}}}{V_{\mathrm{gas}}} \quad (5)$$

where $N_{x,\mathrm{out}}$ is the outlet flow rate of species x [mol h^{-1}]; $C_{x,\mathrm{out}}$ is the outlet gas fraction of species x; $N_{x,\mathrm{in}}$ is the inlet flow rate of species x [mol h^{-1}]; r_x is the formation rate of species x [mmol h^{-1} g$_{\mathrm{cat}}$$^{-1}$]; m_{cat} is the mass of catalyst used in the reaction [g]; X_{CO2} is the conversion rate of CO_2; S_x is the selectivity of species x; t is the contact time [s g mL $^{-1}$]; and V_{gas} is the gas flow rate [mL s^{-1}].

Computational Details

The DFT calculations were performed using the Vienna Ab Initio Simulation Package code.[83] The exchange-correlation function was described through the generalized gradient approximation method in the Perdew−Burke−Ernzerhof[84] form. van der Waals interactions were accounted for using the DFT-D3 method.[85] A cutoff energy of 450 eV was employed, and a vacuum space of 15 Å in the z-direction was set to avoid periodic effects. Γ-centered Monkhorst−Pack K points of 1 × 1 × 1 and 5 × 5 × 1 were employed for geometry optimization and electronic property calculations. In addition, the convergence criteria for energy and force were set to 10^{-5} eV/atom and 0.02 eV/Å, respectively, throughout the calculations. Atomic charges were computed using the atom-in-molecule scheme proposed by Bader.[86] The transition states in the chemical reactions were located through the climbing nudged elastic band (Cl-NEB) method, with a force convergence criterion of 0.05 eV/Å.[87]

For the relative energy, ΔE_{DFT} represents the difference between the two states. The Gibbs free energies can be calculated using the following equation:

$$\Delta G = \Delta E_{\mathrm{DFT}} + \Delta_{\mathrm{ZPE}} + \int C_{\mathrm{p}} \mathrm{d}T - T\Delta S$$

where ΔE_{DFT} is the energy difference calculated by DFT; Δ_{ZPE} is the difference in zero-point energy between reactants and products; $T\Delta S$ and $\int C_{\mathrm{p}} \mathrm{d}T$ represent the contributions of entropic and enthalpic energies at 400 °C (T = 673.15 K). This step analysis was facilitated by the VASPKIT postprocessing software.[88]

■ ASSOCIATED CONTENT

Supporting Information

The Supporting Information is available free of charge at https://pubs.acs.org/doi/10.1021/jacsau.4c01097.

> Additional experimental details, data, and analysis, including photographs of the experimental setup (PDF)

■ AUTHOR INFORMATION

Corresponding Authors

Yayun Zhang − *State Key Laboratory of Chemical Engineering, East China University of Science and Technology, Shanghai 200237, P. R. China;* orcid.org/0000-0002-1714-3126; Email: yy.zhang@ecust.edu.cn

Hui Zhou − *Key Laboratory for Thermal Science and Power Engineering of Ministry of Education, Beijing Key Laboratory of CO2 Utilization and Reduction Technology, Department of Energy and Power Engineering, Tsinghua University, Beijing 100084, P.R. China; Shanxi Research Institute for Clean Energy, Tsinghua University, Shanxi, Taiyuan 030000, P.R. China;* orcid.org/0000-0003-1410-4794; Email: huizhou@tsinghua.edu.cn

Authors

Xuan Bie − *Key Laboratory for Thermal Science and Power Engineering of Ministry of Education, Beijing Key Laboratory of CO2 Utilization and Reduction Technology, Department of Energy and Power Engineering, Tsinghua University, Beijing 100084, P.R. China*

Yukun Pan − *State Key Laboratory of Chemical Engineering, East China University of Science and Technology, Shanghai 200237, P. R. China*

Xiaowei Wang − *State Key Laboratory of Chemical Engineering, East China University of Science and Technology, Shanghai 200237, P. R. China*

Shiyu Zhang − *Key Laboratory for Thermal Science and Power Engineering of Ministry of Education, Beijing Key Laboratory of CO2 Utilization and Reduction Technology, Department of Energy and Power Engineering, Tsinghua University, Beijing 100084, P.R. China*

Jiahui Hu − *New Jersey Institute of Technology, New Jersey 07102, United States*

Xiaoxiao Yang − *Key Laboratory for Thermal Science and Power Engineering of Ministry of Education, Beijing Key Laboratory of CO2 Utilization and Reduction Technology, Department of Energy and Power Engineering, Tsinghua University, Beijing 100084, P.R. China*

Qinghai Li − *Key Laboratory for Thermal Science and Power Engineering of Ministry of Education, Beijing Key Laboratory of CO2 Utilization and Reduction Technology, Department of Energy and Power Engineering, Tsinghua University, Beijing 100084, P.R. China; Shanxi Research Institute for Clean Energy, Tsinghua University, Shanxi, Taiyuan 030000, P.R. China;* orcid.org/0000-0002-5300-9629

Yanguo Zhang − *Key Laboratory for Thermal Science and Power Engineering of Ministry of Education, Beijing Key Laboratory of CO2 Utilization and Reduction Technology, Department of Energy and Power Engineering, Tsinghua University, Beijing 100084, P.R. China; Shanxi Research Institute for Clean Energy, Tsinghua University, Shanxi, Taiyuan 030000, P.R. China*

Robert E. Przekop − *Adam Mickiewicz University, 61-712 Poznań, Poland*

Complete contact information is available at: https://pubs.acs.org/10.1021/jacsau.4c01097

Author Contributions

H.Z. and X.B. conceived the research project. X.B. planned the experimental work. S.Z. prepared the Ni/CeO_2 catalysts. J.H. helped with the charge density analysis. X.Y. assisted the catalyst characterization. Q.L. and Yg.Z. helped with the CO_2 hydrogenation reactions. Yy.Z. designed and supervised the DFT calculations. Y.P. and X.W. performed the DFT calculations. Data were discussed among all coauthors. R.E.P.

assisted in revising the manuscript. Y.P. and Yy.Z. wrote the calculation section, while X.B. and H.Z. wrote the remaining sections with contributions from all authors.

Notes

The authors declare no competing financial interest.

ACKNOWLEDGMENTS

This work was supported by the National Natural Science Foundation of China (52276202, 22478123, and 22008073), National Key R&D Program of China (2023YFC3905701), and Beijing Natural Science Foundation (JQ24053).

REFERENCES

(1) Rickels, W.; Meier, F.; Quaas, M. The Historical Social Cost of Fossil and Industrial CO_2 Emissions. *Nat. Clim. Chang.* **2023**, *13* (7), 742−747.

(2) Masood, E. Net-Zero Carbon Pledges Must Be Meaningful to Avert Climate Disaster. *Nature* **2021**, *592* (7852), 8.

(3) Porosoff, M. D.; Yan, B.; Chen, J. G. Catalytic Reduction of CO_2 by H_2 for Synthesis of CO, Methanol and Hydrocarbons: Challenges and Opportunities. *Energy Environ. Sci.* **2016**, *9* (1), 62−73.

(4) Kang, H.; Zhu, L.; Li, S.; Yu, S.; Niu, Y.; Zhang, B.; Chu, W.; Liu, X.; Perathoner, S.; Centi, G.; Liu, Y. Generation of Oxide Surface Patches Promoting H-Spillover in Ru/(TiO_x)MnO Catalysts Enables CO_2 Reduction to CO. *Nat. Catal.* **2023**, *6*, 1062−1072.

(5) Navarro, V.; Van Spronsen, M. A.; Frenken, J. W. M. In Situ Observation of Self-Assembled Hydrocarbon Fischer−Tropsch Products on a Cobalt Catalyst. *Nat. Chem.* **2016**, *8* (10), 929−934.

(6) Centi, G.; Quadrelli, E. A.; Perathoner, S. Catalysis for CO_2 Conversion: A Key Technology for Rapid Introduction of Renewable Energy in the Value Chain of Chemical Industries. *Energy Environ. Sci.* **2013**, *6* (6), 1711−1731.

(7) Sikarwar, V. S.; Zhao, M.; Clough, P.; Yao, J.; Zhong, X.; Memon, M. Z.; Shah, N.; Anthony, E. J.; Fennell, P. S. An Overview of Advances in Biomass Gasification. *Energy Environ. Sci.* **2016**, *9* (10), 2939−2977.

(8) Moustakas, K.; Parmaxidou, P.; Vakalis, S. Anaerobic Digestion for Energy Production from Agricultural Biomass Waste in Greece: Capacity Assessment for the Region of Thessaly. *Energy* **2020**, *191*, No. 116556.

(9) Zamri, M. F. M. A.; Hasmady, S.; Akhiar, A.; Ideris, F.; Shamsuddin, A. H.; Mofijur, M.; Fattah, I. M. R.; Mahlia, T. M. I. A Comprehensive Review on Anaerobic Digestion of Organic Fraction of Municipal Solid Waste. *Renew. Sustain. Energy Rev.* **2021**, *137* (December 2020), No. 110637.

(10) Liu, S.; Li, H.; Zhang, K.; Lau, H. C. Techno-Economic Analysis of Using Carbon Capture and Storage (CCS) in Decarbonizing China's Coal-Fired Power Plants. *J. Clean. Prod.* **2022**, *351* (September 2021), No. 131384.

(11) Olabi, A. G.; Wilberforce, T.; Elsaid, K.; Sayed, E. T.; Maghrabie, H. M.; Abdelkareem, M. A. Large Scale Application of Carbon Capture to Process Industries − A Review. *J. Clean. Prod.* **2022**, *362* (September 2021), No. 132300.

(12) Torres, W.; Pansare, S. S.; Goodwin, J. G. Hot Gas Removal of Tars, Ammonia, and Hydrogen Sulfide from Biomass Gasification Gas. *Catal. Rev. - Sci. Eng.* **2007**, *49* (4), 407−456.

(13) Laudenschleger, D.; Ruland, H.; Muhler, M. Identifying the Nature of the Active Sites in Methanol Synthesis over Cu/ZnO/Al2O3 Catalysts. *Nat. Commun.* **2020**, *11* (1), 3898.

(14) Porter, R. T. J.; Fairweather, M.; Pourkashanian, M.; Woolley, R. M. The Range and Level of Impurities in CO_2 Streams from Different Carbon Capture Sources. *Int. J. Greenh. Gas Control* **2015**, *36*, 161−174.

(15) Wetenhall, B.; Aghajani, H.; Chalmers, H.; Benson, S. D.; Ferrari, M. C.; Li, J.; Race, J. M.; Singh, P.; Davison, J. Impact of CO_2 Impurity on CO_2 Compression, Liquefaction and Transportation. *Energy Procedia* **2014**, *63*, 2764−2778.

(16) Barrientos, J.; Montes, V.; Boutonnet, M.; Järås, S. Further Insights into the Effect of Sulfur on the Activity and Selectivity of Cobalt-Based Fischer−Tropsch Catalysts. *Catal. Today* **2016**, *275*, 119−126.

(17) Jiang, F.; Wang, S.; Liu, B.; Liu, J.; Wang, L.; Xiao, Y.; Xu, Y.; Liu, X. Insights into the Influence of CeO_2 Crystal Facet on CO_2 Hydrogenation to Methanol over Pd/CeO_2 Catalysts. *ACS Catal.* **2020**, *10*, 11493−11509.

(18) de Oliveira, D. C.; Lora, E. E. S.; Venturini, O. J.; Maya, D. M. Y.; Garcia-Pérez, M. Gas Cleaning Systems for Integrating Biomass Gasification with Fischer−Tropsch Synthesis - A Review of Impurity Removal Processes and Their Sequences. *Renew. Sustain. Energy Rev.* **2023**, *172* (November 2022), No. 113047.

(19) Asadullah, M. Biomass Gasification Gas Cleaning for Downstream Applications: A Comparative Critical Review. *Renew. Sustain. Energy Rev.* **2014**, *40*, 118−132.

(20) Yang, C.; Yang, S.; Fan, H. L.; Wang, J.; Wang, H.; Shangguan, J.; Huo, C. A Sustainable Design of ZnO-Based Adsorbent for Robust H_2S Uptake and Secondary Utilization as Hydrogenation Catalyst. *Chem. Eng. J.* **2020**, *382* (June 2019), No. 122892.

(21) Wang, Y.; Gao, W.; Li, K.; Zheng, Y.; Xie, Z.; Na, W.; Chen, J. G.; Wang, H. Strong Evidence of the Role of H_2O in Affecting Methanol Selectivity from CO_2 Hydrogenation over Cu-ZnO-ZrO_2. *Chem.* **2020**, *6* (2), 419−430.

(22) Zhao, Y. F.; Yang, Y.; Mims, C.; Peden, C. H. F.; Li, J.; Mei, D. Insight into Methanol Synthesis from CO_2 Hydrogenation on Cu(111): Complex Reaction Network and the Effects of H_2O. *J. Catal.* **2011**, *281* (2), 199−211.

(23) Beale, A. M.; Gibson, E. K.; O'Brien, M. G.; Jacques, S. D. M.; Cernik, R. J.; Michiel, M. D.; Cobden, P. D.; Pirgon-Galin, Ö.; Water, L. v. d.; Watson, M. J.; Weckhuysen, B. M. Chemical Imaging of the Sulfur-Induced Deactivation of Cu/ZnO Catalyst Bodies. *J. Catal.* **2014**, *314*, 94−100.

(24) Rao Pendyala, V. R.; Shafer, W. D.; Jacobs, G.; Martinelli, M.; Sparks, D. E.; Davis, B. H. Fischer−Tropsch Synthesis: Effect of Ammonia on Product Selectivities for a Pt Promoted Co/Alumina Catalyst. *RSC Adv.* **2017**, *7* (13), 7793−7800.

(25) Rausch, A. K.; Schubert, L.; Henkel, R.; van Steen, E.; Claeys, M.; Roessner, F. Enhanced Olefin Production in Fischer−Tropsch Synthesis Using Ammonia Containing Synthesis Gas Feeds. *Catal. Today* **2016**, *275*, 94−99.

(26) Kizilkaya, A. C.; Niemantsverdriet, J. W.; Weststrate, C. J. Ammonia Adsorption and Decomposition on Co(0001) in Relation to Fischer−Tropsch Synthesis. *J. Phys. Chem. C* **2016**, *120* (7), 3834−3845.

(27) Ma, W.; Jacobs, G.; Sparks, D. E.; Pendyala, V. R. R.; Hopps, S. G.; Thomas, G. A.; Hamdeh, H. H.; Maclennan, A.; Hu, Y.; Davis, B. H. Fischer−Tropsch Synthesis: Effect of Ammonia in Syngas on the Fischer−Tropsch Synthesis Performance of a Precipitated Iron Catalyst. *J. Catal.* **2015**, *326*, 149−160.

(28) Clark, Y. A., Process of Synthesizing Aliphatic Amines, US 2548,754 A, 1950.

(29) Grabow, L. C.; Mavrikakis, M. Mechanism of Methanol Synthesis on Cu through CO_2 and CO Hydrogenation. *ACS Catal.* **2011**, *1* (4), 365−384.

(30) Meunier, F. C. Mixing Copper Nanoparticles and ZnO Nanocrystals: A Route towards Understanding the Hydrogenation of CO_2 to Methanol? *Angew. Chemie - Int. Ed.* **2011**, *50* (18), 4053−4054.

(31) Liao, F.; Huang, Y.; Ge, J.; Zheng, W.; Tedsree, K.; Collier, P.; Hong, X.; Tsang, S. C. Morphology-Dependent Interactions of ZnO with Cu Nanoparticles at the Materials' Interface in Selective Hydrogenation of CO_2 to CH_3OH. *Angew. Chemie - Int. Ed.* **2011**, *50* (9), 2162−2165.

(32) Beck, A.; Zabilskiy, M.; Newton, M. A.; Safonova, O.; Willinger, M. G.; van Bokhoven, J. A. Following the Structure of Copper-Zinc-Alumina across the Pressure Gap in Carbon Dioxide Hydrogenation. *Nat. Catal.* **2021**, *4* (6), 488−497.

(33) Zhang, H.; Chen, J.; Han, X.; Pan, Y.; Hao, Z.; Tang, S.; Zi, X.; Zhang, Z.; Gao, P.; Li, M.; Lv, J.; Ma, X. High-Performance Cu/ZnO/Al_2O_3 Catalysts for CO_2 Hydrogenation to Methanol. *Ind. Eng. Chem. Res.* **2024**, *63* (14), 6210−6221.

(34) Behrens, M.; Studt, F.; Kasatkin, I.; Kühl, S.; Hävecker, M.; Abild-Pedersen, F.; Zander, S.; Girgsdies, F.; Kurr, P.; Kniep, B. L.; Tovar, M.; Fischer, R. W.; Nørskov, J. K.; Schlögl, R. The Active Site of Methanol Synthesis over Cu/ZnO/Al_2O_3 Industrial Catalysts. *Science.* **2012**, *336* (May), 893−898.

(35) Ma, L.; Cheng, Y.; Cavataio, G.; McCabe, R. W.; Fu, L.; Li, J. In Situ DRIFTS and Temperature-Programmed Technology Study on NH_3-SCR of NO_x over Cu-SSZ-13 and Cu-SAPO-34 Catalysts. *Appl. Catal. B Environ.* **2014**, *156*−*157*, 428−437.

(36) Yan, L.; Ji, Y.; Wang, P.; Feng, C.; Han, L.; Li, H.; Yan, T.; Shi, L.; Zhang, D. Alkali and Phosphorus Resistant Zeolite-like Catalysts for NOxReduction by NH3. *Environ. Sci. Technol.* **2020**, *54* (14), 9132−9141.

(37) Li, S.; Xu, Y.; Wang, H.; Teng, B.; Liu, Q.; Li, Q.; Xu, L.; Liu, X.; Lu, J. Tuning the CO_2 Hydrogenation Selectivity of Rhodium Single-Atom Catalysts on Zirconium Dioxide with Alkali Ions. *Angew. Chem. Int. Ed.* **2023**, *62* (8), 1−8.

(38) Wu, Q.; Li, H.; Yang, G.; Cao, Y.; Wang, H.; Peng, F.; Yu, H. Surface Intermediates Steer the Pathways of CO_2 Hydrogenation on Pt/γ-Al_2O_3: Importance of the Metal-Support Interface. *J. Catal.* **2023**, *425*, 40−49.

(39) Yoo, C. J.; Getsoian, A. (.; Bhan, A. NH_3 Formation Pathways from NO Reduction by CO in the Presence of Water over Rh/Al_2O_3. *Appl. Catal. B Environ.* **2021**, *286* (0), No. 119893.

(40) Zhang, Y.; Wu, B.; Xu, Y.; Wu, Y.; Yang, W.; Huang, C.; Wang, X.; Zhong, L.; Wang, J.; Chen, Y. The Formation Mechanism of N_2O and NH_3 on PtRh Three-Way Catalyst of Natural Gas Vehicles. *Mol. Catal.* **2023**, *547* (April), No. 113392.

(41) Ihli, J.; Wong, W. C.; Noel, E. H.; Kim, Y. Y.; Kulak, A. N.; Christenson, H. K.; Duer, M. J.; Meldrum, F. C. Dehydration and Crystallization of Amorphous Calcium Carbonate in Solution and in Air. *Nat. Commun.* **2014**, *5*, 1−10.

(42) Larmier, K.; Liao, W. C.; Tada, S.; Lam, E.; Verel, R.; Bansode, A.; Urakawa, A.; Comas-Vives, A.; Copéret, C. CO_2-to-Methanol Hydrogenation on Zirconia-Supported Copper Nanoparticles: Reaction Intermediates and the Role of the Metal−Support Interface. *Angew. Chemie - Int. Ed.* **2017**, *56* (9), 2318−2323.

(43) Cheng, H. N.; Wartelle, L. H.; Klasson, K. T.; Edwards, J. C. Solid-State NMR and ESR Studies of Activated Carbons Produced from Pecan Shells. *Carbon N. Y.* **2010**, *48* (9), 2455−2469.

(44) Ishihara, S.; Sahoo, P.; Deguchi, K.; Ohki, S.; Tansho, M.; Shimizu, T.; Labuta, J.; Hill, J. P.; Ariga, K.; Watanabe, K.; Yamauchi, Y.; Suehara, S.; Iyi, N. Dynamic Breathing of Co_2 by Hydrotalcite. *J. Am. Chem. Soc.* **2013**, *135* (48), 18040−18043.

(45) Zhou, H.; Docherty, S. R.; Phongprueksathat, N.; Chen, Z.; Bukhtiyarov, A. V.; Prosvirin, I. P.; Safonova, O. V.; Urakawa, A.; Copéret, C.; Müller, C. R.; Fedorov, A. Combining Atomic Layer Deposition with Surface Organometallic Chemistry to Enhance Atomic-Scale Interactions and Improve the Activity and Selectivity of Cu-Zn/SiO_2 Catalysts for the Hydrogenation of CO_2 to Methanol. *JACS Au* **2023**, *3* (9), 2536−2549.

(46) Zhao, Y. H.; Horita, Z.; Langdon, T. G.; Zhu, Y. T. Evolution of Defect Structures during Cold Rolling of Ultrafine-Grained Cu and Cu-Zn Alloys: Influence of Stacking Fault Energy. *Mater. Sci. Eng., A* **2008**, *474* (1−2), 342−347.

(47) Divins, N. J.; Kordus, D.; Timoshenko, J.; Sinev, I.; Zegkinoglou, I.; Bergmann, A.; Chee, S. W.; Widrinna, S.; Karslıoğlu, O.; Mistry, H.; Lopez Luna, M.; Zhong, J. Q.; Hoffman, A. S.; Boubnov, A.; Boscoboinik, J. A.; Heggen, M.; Dunin-Borkowski, R. E.; Bare, S. R.; Cuenya, B. R. Operando High-Pressure Investigation of Size-Controlled CuZn Catalysts for the Methanol Synthesis Reaction. *Nat. Commun.* **2021**, *12* (1), 1435.

(48) Sun, J. T.; Metcalfe, I. S.; Sahibzada, M. Deactivation of Cu/ZnO/Al_2O_3 Methanol Synthesis Catalyst by Sintering. *Ind. Eng. Chem. Res.* **1999**, *38* (10), 3868−3872.

(49) Zhao, H.; Yu, R.; Ma, S.; Xu, K.; Chen, Y.; Jiang, K.; Fang, Y.; Zhu, C.; Liu, X.; Tang, Y.; Wu, L.; Wu, Y.; Jiang, Q.; He, P.; Liu, Z.; Tan, L. The Role of Cu_1-O_3 Species in Single-Atom Cu/ZrO_2 Catalyst for CO_2 Hydrogenation. *Nat. Catal.* **2022**, *5*, 818−831.

(50) Bhardwaj, R.; Bharti, A.; Singh, J. P.; Chae, K. H.; Goyal, N. Influence of Cu Doping on the Local Electronic and Magnetic Properties of ZnO Nanostructures. *Nanoscale Adv.* **2020**, *2* (10), 4450−4463.

(51) Zabilskiy, M.; Sushkevich, V. L.; Palagin, D.; Newton, M. A.; Krumeich, F.; van Bokhoven, J. A. The Unique Interplay between Copper and Zinc during Catalytic Carbon Dioxide Hydrogenation to Methanol. *Nat. Commun.* **2020**, *11* (1), 1−8.

(52) Zhu, Y.; Zheng, J.; Ye, J.; Cui, Y.; Koh, K.; Kovarik, L.; Camaioni, D. M.; Fulton, J. L.; Truhlar, D. G.; Neurock, M.; Cramer, C. J.; Gutiérrez, O. Y.; Lercher, J. A. Copper-Zirconia Interfaces in UiO-66 Enable Selective Catalytic Hydrogenation of CO_2 to Methanol. *Nat. Commun.* **2020**, *11* (1), 1−11.

(53) Wang, Y.; Kattel, S.; Gao, W.; Li, K.; Liu, P.; Chen, J. G.; Wang, H. Exploring the Ternary Interactions in Cu−ZnO−ZrO_2 Catalysts for Efficient CO_2 Hydrogenation to Methanol. *Nat. Commun.* **2019**, *10* (1), 1166.

(54) Lunkenbein, T.; Schumann, J.; Behrens, M.; Schlögl, R.; Willinger, M. G. Formation of a ZnO Overlayer in Industrial Cu/ZnO/Al_2O_3 Catalysts Induced by Strong Metal−Support Interactions. *Angew. Chemie Int. Ed.* **2015**, *54* (15), 4544−4548.

(55) Chen, Z.; Wen, J.; Zeng, Y.; Li, M.; Tian, Y.; Yang, F.; Li, M. M. J.; Chen, P.; Huang, H.; Ye, D.; Chen, L. The Origin of the Mediocre Methanol Selectivity of Cu/ZnO-Based Catalysts for Methanol Synthesis from CO_2 Hydrogenation. *Appl. Catal. B Environ.* **2024**, *340* (May 2023), No. 123192.

(56) Liu, X.; Luo, J.; Wang, H.; Huang, L.; Wang, S.; Li, S.; Sun, Z. In Situ Spectroscopic Characterization and Theoretical Calculations Identify Partially Reduced ZnO_{1-x}/Cu Interfaces for Methanol Synthesis from CO_2 Results and Discussion. *leAngew. Chem., Int. Ed.* **2022**, *61*, No. e202202330.

(57) Liu, X.; Wang, H.; Lu, J. Recent Progress in Understanding the Nature of Active Sites for Methanol Synthesis over Cu/ZnO Catalysts. *J. Catal.* **2024**, *436*, No. 115561.

(58) Le Valant, A.; Comminges, C.; Tisseraud, C.; Canaff, C.; Pinard, L.; Pouilloux, Y. The Cu-ZnO Synergy in Methanol Synthesis from CO_2, Part 1: Origin of Active Site Explained by Experimental Studies and a Sphere Contact Quantification Model on Cu + ZnO Mechanical Mixtures. *J. Catal.* **2015**, *324*, 41−49.

(59) Tisseraud, C.; Comminges, C.; Belin, T.; Ahouari, H.; Soualah, A.; Pouilloux, Y.; Le Valant, A. The Cu-ZnO Synergy in Methanol Synthesis from CO_2, Part 2: Origin of the Methanol and CO Selectivities Explained by Experimental Studies and a Sphere Contact Quantification Model in Randomly Packed Binary Mixtures on Cu-ZnO Coprecipitate Catalysts. *J. Catal.* **2015**, *330*, 533−544.

(60) Kattel, S.; Ramírez, P. J.; Chen, J. G.; Rodriguez, J. A.; Liu, P. Active Sites for CO_2 Hydrogenation to Methanol on Cu/ZnO Catalysts. *Science.* **2017**, *355* (6331), 1296−1299.

(61) Ye, R.; Ma, L.; Mao, J.; Wang, X.; Hong, X.; Gallo, A.; Ma, Y.; Luo, W.; Wang, B.; Zhang, R.; Duyar, M. S.; Jiang, Z.; Liu, J. A Ce-CuZn Catalyst with Abundant Cu/Zn-O_V-Ce Active Sites for CO_2 Hydrogenation to Methanol. *Nat. Commun.* **2024**, *15* (1), 2159.

(62) Kuld, S.; Conradsen, C.; Moses, P. G.; Chorkendorff, I.; Sehested, J. Quantification of Zinc Atoms in a Surface Alloy on Copper in an Industrial-Type Methanol Synthesis Catalyst. *Angew. Chemie - Int. Ed.* **2014**, *53* (23), 5941−5945.

(63) Hu, B.; Yin, Y.; Liu, G.; Chen, S.; Hong, X.; Tsang, S. C. E. Hydrogen Spillover Enabled Active Cu Sites for Methanol Synthesis from CO_2 Hydrogenation over Pd Doped CuZn Catalysts. *J. Catal.* **2018**, *359*, 17−26.

(64) Xiong, W.; Wu, Z.; Chen, X.; Ding, J.; Ye, A.; Zhang, W.; Huang, W. Active Copper Structures in ZnO-Cu Interfacial Catalysis: CO_2 Hydrogenation to Methanol and Reverse Water-Gas Shift Reactions. *Sci. China Chem.* **2024**, *67* (2), 715−723.

(65) Pritchard, J.; Catterick, T.; Gupta, R. K. Infrared Spectroscopy of Chemisorbed Carbon Monoxide on Copper. *Surf. Sci.* **1975**, *53* (1), 1−20.

(66) Kuld, S.; Thorhauge, M.; Falsig, H.; Elkjær, C. F.; Helveg, S.; Chorkendorff, I.; Sehested, J. Quantifying the Promotion of Cu Catalysts by ZnO for Methanol Synthesis. *Science* **2016**, *352* (April), 969.

(67) Amann, P.; Klötzer, B.; Degerman, D.; Köpfle, N.; Götsch, T.; Lömker, P.; Rameshan, C.; Ploner, K.; Bikaljevic, D.; Wang, H.; Soldemo, M.; Shipilin, M.; Goodwin, C. M.; Gladh, J. The State of Zinc in Methanol Synthesis over a Zn/ZnO/Cu(211) Model Catalyst. *Science* **2022**, *211*, 603−608.

(68) Martin, O.; Mondelli, C.; Cervellino, A.; Ferri, D.; Curulla-Ferré, D.; Pérez-Ramírez, J. Operando Synchrotron X-Ray Powder Diffraction and Modulated-Excitation Infrared Spectroscopy Elucidate the CO2Promotion on a Commercial Methanol Synthesis Catalyst. *Angew. Chemie - Int. Ed.* **2016**, *55* (37), 11031−11036.

(69) Arandia, A.; Yim, J.; Warraich, H.; Leppäkangas, E.; Bes, R.; Lempelto, A.; Gell, L.; Jiang, H.; Meinander, K.; Viinikainen, T.; Huotari, S.; Honkala, K.; Puurunen, R. L. Effect of Atomic Layer Deposited Zinc Promoter on the Activity of Copper-on-Zirconia Catalysts in the Hydrogenation of Carbon Dioxide to Methanol. *Appl. Catal. B Environ.* **2023**, *321* (October 2022), No. 122046.

(70) Noei, H.; Wöll, C.; Muhler, M.; Wang, Y. Activation of Carbon Dioxide on ZnO Nanoparticles Studied by Vibrational Spectroscopy. *J. Phys. Chem. C* **2011**, *115* (4), 908−914.

(71) Tang, Y.; Yang, Z.; Guo, C.; Han, H.; Jiang, Y.; Wang, Z.; Liu, J.; Wu, L.; Wang, F. Encapsulating Ir Nanoparticles into UiO-66 for Photo-Thermal Catalytic CO_2 Methanation under Ambient Pressure. *J. Mater. Chem. A* **2022**, *10* (22), 12157−12167.

(72) Mukherjee, S.; Devaguptapu, S. V.; Sviripa, A.; Lund, C. R. F.; Wu, G. Low-Temperature Ammonia Decomposition Catalysts for Hydrogen Generation. *Appl. Catal. B Environ.* **2018**, *226* (December 2017), 162−181.

(73) Sun, S.; Jiang, Q.; Zhao, D.; Cao, T.; Sha, H.; Zhang, C.; Song, H.; Da, Z. Ammonia as Hydrogen Carrier: Advances in Ammonia Decomposition Catalysts for Promising Hydrogen Production. *Renew. Sustain. Energy Rev.* **2022**, *169*, No. 112918.

(74) Zhou, J.; Gao, Z.; Xiang, G.; Zhai, T.; Liu, Z.; Zhao, W.; Liang, X.; Wang, L. Interfacial Compatibility Critically Controls Ru/TiO_2 Metal-Support Interaction Modes in CO_2 Hydrogenation. *Nat. Commun.* **2022**, *13* (1), 1−10.

(75) Tang, X.; Song, C.; Li, H.; Liu, W.; Hu, X.; Chen, Q.; Lu, H.; Yao, S.; Li, X.; Lin, L. Thermally Stable Ni Foam-Supported Inverse CeAlOx/Ni Ensemble as an Active Structured Catalyst for CO_2 Hydrogenation to Methane. *Nat. Commun.* **2024**, *15*, 3115.

(76) Zheng, W.; Cotter, T. P.; Kaghazchi, P.; Jacob, T.; Frank, B.; Schlichte, K.; Zhang, W.; Su, D. S.; Schüth, F.; Schlögl, R. Experimental and Theoretical Investigation of Molybdenum Carbide and Nitride as Catalysts for Ammonia Decomposition. *J. Am. Chem. Soc.* **2013**, *135* (9), 3458−3464.

(77) Liu, H.; Zhang, Y.; Liu, S.; Li, S.; Liu, G. Ni-CeO_2 Nanocomposite with Enhanced Metal-Support Interaction for Effective Ammonia Decomposition to Hydrogen. *Chem. Eng. J.* **2023**, *473* (July), No. 145371.

(78) Wang, X.; Shi, H.; Kwak, J. H.; Szanyi, J. Mechanism of CO2 Hydrogenation on Pd/Al_2O_3 Catalysts: Kinetics and Transient DRIFTS-MS Studies. *ACS Catal.* **2015**, *5* (11), 6337−6349.

(79) Muravev, V.; Spezzati, G.; Su, Y. Q.; Parastaev, A.; Chiang, F. K.; Longo, A.; Escudero, C.; Kosinov, N.; Hensen, E. J. M. Interface Dynamics of Pd−CeO_2 Single-Atom Catalysts during CO Oxidation. *Nat. Catal.* **2021**, *4* (6), 469−478.

(80) Zhang, X.; Zhu, X.; Lin, L.; Yao, S.; Zhang, M.; Liu, X.; Wang, X.; Li, Y. W.; Shi, C.; Ma, D. Highly Dispersed Copper over β-Mo_2C as an Efficient and Stable Catalyst for the Reverse Water Gas Shift (RWGS) Reaction. *ACS Catal.* **2017**, *7* (1), 912−918.

(81) Thommes, M.; Kaneko, K.; Neimark, A. V.; Olivier, J. P.; Rodriguez-Reinoso, F.; Rouquerol, J.; Sing, K. S. W. Physisorption of Gases, with Special Reference to the Evaluation of Surface Area and Pore Size Distribution (IUPAC Technical Report). *Pure Appl. Chem.* **2015**, *87* (9−10), 1051−1069.

(82) Ravel, B.; Newville, M. ATHENA, ARTEMIS, HEPHAESTUS: Data Analysis for X-Ray Absorption Spectroscopy Using IFEFFIT. *J. Synchrotron Radiat.* **2005**, *12* (4), 537−541.

(83) Kresse, G.; Furthmüller, J. Efficiency of Ab-Initio Total Energy Calculations for Metals and Semiconductors Using a Plane-Wave Basis Set. *Comput. Mater. Sci.* **1996**, *6* (1), 15−50.

(84) Perdew, J. P.; Burke, K.; Ernzerhof, M. Generalized Gradient Approximation Made Simple. *Phys. Rev. Lett.* **1996**, *77* (18), 3865−3868.

(85) Grimme, S.; Antony, J.; Ehrlich, S.; Krieg, H. A Consistent and Accurate Ab Initio Parametrization of Density Functional Dispersion Correction (DFT-D) for the 94 Elements H-Pu. *J. Chem. Phys.* **2010**, *132* (15), No. 154104.

(86) Bader, R. F. W. A Quantum Theory of Molecular Structure and Its Applications. *Chem. Rev.* **1991**, *91* (5), 893−928.

(87) Henkelman, G.; Uberuaga, B. P.; Jónsson, H. A Climbing Image Nudged Elastic Band Method for Finding Saddle Points and Minimum Energy Paths. *J. Chem. Phys.* **2000**, *113* (22), 9901−9904.

(88) Wang, V.; Xu, N.; Liu, J. C.; Tang, G.; Geng, W. T. VASPKIT: A User-Friendly Interface Facilitating High-Throughput Computing and Analysis Using VASP Code. *Comput. Phys. Commun.* **2021**, *267*, No. 108033.